

BTE-Barna: An extension of almaBTE for thermal simulation of devices based on 2D materials

Martí Raya-Moreno^a, Xavier Cartoixà^a, Jesús Carrete^{b,*}

^aDepartament d'Enginyeria Electrònica, Universitat Autònoma de Barcelona, 08193 Bellaterra, Barcelona, Spain

^bInstitute of Materials Chemistry, TU Wien, A-1060 Vienna, Austria

Abstract

We present BTE-Barna (Boltzmann Transport Equation - Beyond the Rta for NANosystems), a software package that extends the Monte Carlo (MC) module of the almaBTE solver of the Peierls-Boltzmann transport equation for phonons (PBTE) to work with nanosystems based on 2D materials with complex geometries. To properly capture how the phonon occupations evolve in momentum space as a result of scattering, we have supplemented the relaxation-time approximation with an implementation of the propagator for the full linearized version of the PBTE. The code can now find solutions for finite and extended devices under the effect of a thermal gradient, with isothermal reservoirs or with an arbitrary initial temperature distribution in space and time, writing out the temperature and heat flux distributions as well as their spectral decompositions. Besides the full deviational MC solver, a number of useful approximations for highly symmetric devices are also included.

Keywords: Phonons; Boltzmann transport equation; 2D materials

PROGRAM SUMMARY

Program Title: BTE-Barna

CPC Library link to program files: (to be added by Technical Editor)

Developer's repository link: <https://github.com/sousaw/BTE-Barna>

Code Ocean capsule: (to be added by Technical Editor)

Licensing provisions: Apache-2.0

Programming language: C++

Nature of problem: Calculation of temperature profiles, thermal flux and/or effective thermal conductivities for nanosystems based on 2D materials.

Solution method:

For highly symmetric systems confined along some direction(s), the linearized phonon Boltzmann transport equation is solved iteratively by partially suppressing the phonon lifetimes due to boundaries. For more complex geometries, an energy-based deviational Monte Carlo method including off-diagonal terms in the linearized scattering operator arising from the phonon-phonon interaction is used.

Additional comments including restrictions and unusual features:

Depends on the following external libraries: boost, Eigen, HDF5, MessagePack, MPI, oneTBB, spglib, and almaBTE.

1. Introduction

The continuous shrinking of electronic components, following Moore's Law [1], is pushing bulk semiconductor-based devices, such as silicon transistors, to their fundamental limits. In addition, this increase in the integration level leads to ever higher power densities and raises the Herculean challenge of dissipating the generated heat [2].

In this context, two dimensional materials (2DMs), thanks to their atomic thickness, low surface roughness and density of dangling bonds [3], together with the possibility of stacking them to create heterostructures with tuned properties and their compatibility with CMOS technology, are quite promising candidates to replace III-V compounds and silicon in transistor channels [4, 5]. Understanding thermal transport in 2DMs is essential to optimize heat management in such devices. Since phonons are the main heat carriers in semiconductors, heat flux can be described through the Peierls-Boltzmann Transport Equation (PBTE) [6]. For highly symmetric structures (e.g.: bulk systems, nanowires, thin-films...) the relaxation time approximation (RTA), where it is assumed that each phonon mode relaxes to equilibrium independently, has a long tradition of being used, but more recent advances enable an iterative solution beyond that crude approximation [7, 8]. Furthermore, the inclusion of phonon properties calculated from first-principles (frequencies, scattering rates...) makes it possible to solve the PBTE even for novel materials where simpler models to describe those properties are lacking [9, 10]. These iterative first-principles-based PBTE solvers are available to

*Corresponding author.

E-mail address: jesus.carrete.montana@tuwien.ac.at

the community in software packages such as **ShengBTE** [11], **almaBTE** [12] or **Phono3py** [13].

Despite those advances in solving the PBTE for simple systems, using direct or iterative methods for its solution becomes impractical for more intricate configurations, such as the ones required by micro or nanosized devices. A usual approach to overcome such limitations is to use a Monte Carlo method to integrate the PBTE. Notwithstanding their success in other applications, in classical Monte Carlo methods to solve the PBTE the accuracy is hindered by several factors, most notably the inability of the scattering algorithm to conserve energy. Indeed, additional algorithms are required to keep the system energy constant [14, 15, 16], which can bias the distribution in unknown ways [17]. Moreover, classical methods suffer from high statistical noise plus the fact that most of the computational time is wasted simulating the equilibrium part of the distribution [12, 18, 17]. In that context, RTA-based deviational energy Monte Carlo methods have proven themselves as good alternative ways to overcome the limitations [18, 19, 17] of more traditional methods, as they naturally conserve the energy by operating with bundles of energy instead of phonons and reduce the required number of computational particles by simulating only the deviation from a reference equilibrium distribution.

However, the validity of the RTA approach for 2D materials is questionable, and it has been shown to yield a very poor description of thermal properties for several of them [20, 21]. For those cases one might need to use an energy deviational Monte Carlo method based on the full collision operator [22].

In this work we present the **BTE-Barna** software package, an extension of **almaBTE** to tackle 2D systems both within and beyond the RTA, so that now it can address finite and/or periodic 2D materials and their heterojunctions under the effect of thermal gradients and isothermal reservoirs. We analyze a selection of test cases and discuss the validity of the RTA. Additionally, the iterative solver in **almaBTE** is extended to provide the effective thermal conductivity for nanoribbons and nanowires.

The paper is structured as follows: after displaying the general structure of **BTE-Barna** in Sec. 2 and discussing the theoretical background in Sec. 3, we provide test cases of the implementation in Sec. 4 and present illustrative example applications of our package simulators in Sec. 5. Our summary and conclusions are given in Sec. 6. The appendices provide a discussion about the solution of the PBTE in nanowires, additional examples and detailed documentation.

2. BTE-Barna structure

Fig. 1 shows the different pieces of **BTE-Barna** package and how they relate to each other. The whole package heavily relies on **almaBTE** library routines, which have been extended to allow for the solution of PBTE in finite devices based on 2D materials. Moreover, all the executables

use the mode-resolved phonon properties as inputs, which are read from **almaBTE**-generated HDF5 files. A more detailed explanation of all the executables, their inputs, and outputs can be found in the Appendix A for the iterative solver, and in Appendix B for the Monte Carlo solvers, their input generators, and post-processing tools.

3. Methodology

3.1. Effective thermal conductivity for nanoribbons

Despite the fact that an exact solution of the PBTE for highly symmetric systems like nanoribbons or nanowires would require a discretization in space, it is possible to obtain an approximate solution by using averages under the assumption of fully dispersive boundaries [8]. In such a way, it becomes possible to obtain an effective thermal conductivity (κ_{nano}) by simply introducing suppression factors in the lifetimes ($\tau_{\lambda}^{\text{nano}} = \tau_{\lambda}^0 S_{\lambda}^{\text{nano}}$) and then solving the PBTE like in bulk under homogeneous gradients [11].

For nanoribbons contained in the XY plane, the suppression factors (S_{λ}^{nr}) can be calculated by evaluating the integrals in Eq. (8) of Ref. 8 (see Appendix C for nanowires), obtaining:

$$S_{\lambda}^{\text{nr}} = 1 + \left[\frac{M_{\lambda}^{\text{nr}}}{L} \left(e^{-\frac{L}{M_{\lambda}^{\text{nr}}}} - 1 \right) \right] \quad (1)$$

$$M_{\lambda}^{\text{nr}} = \left| \left[\begin{pmatrix} u_y & u_x \\ -u_x & u_y \end{pmatrix}^{-1} v_{\lambda} \right] \cdot e_1 \right| \tau_{\lambda}, \quad (2)$$

where u is a normalized vector pointing along the unbounded direction of the system, v_{λ} and τ_{λ} are the velocity and bulk lifetime of λ -th mode, L is the nanoribbon width and e_1 is the first column of identity matrix. Details on implementation, executable, inputs and outputs can be found in Appendix A.

3.2. RTA Monte Carlo

The implementation for 2D materials of the RTA Monte Carlo is based on code already in **almaBTE** [12], whose formulation was proposed by Péraud *et al.* [19]. The algorithm simulates the space and time evolution of deviational power (emitted by sources and absorbed by sinks) by splitting its distribution into discrete packets—the deviational particles—and tracking their trajectories in a linearized regime. The validity of the existing implementation rests on the assumption that differences in temperature are small enough that a single reference temperature can be defined for the whole system. We now take a look at the main improvements of our code upon that baseline; see Appendix D for a detailed explanation of the whole algorithm.

The original implementation, **steady_montecarlo1d**, was designed to investigate one-dimensional steady-state situations in materials/heterostructures embedded between two isothermal reservoirs having the same cross section, which owing to finite thickness might not be true for

BTE-Barna

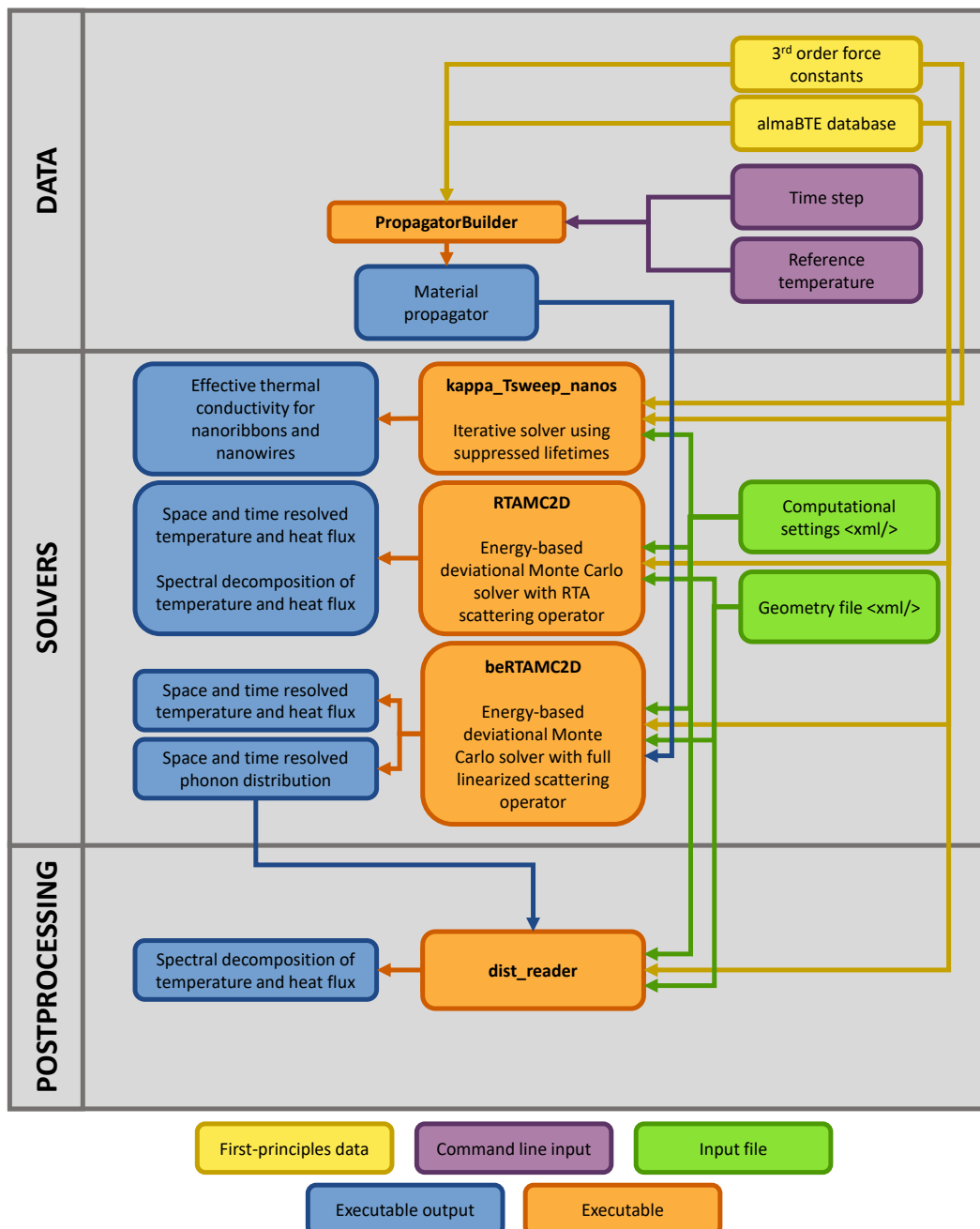


Figure 1: General structure of BTE-Barna package.

2D-material-based systems/devices. Consequently, we extended the geometric algorithms to deal with 2D systems using the boost::geometry library [23]. In this implementation the system is composed of different computational boxes, which are defined by the user as convex hulls of points, therefore enabling the creation of complex geometries. Additionally, as the finiteness of real 2D devices requires dealing with boundary scattering, we implemented a full diffusive condition in which the out-state is randomly selected from a Lambert cosine law distribution [24] defined by transition probabilities from a state i to f :

$$P_{i \rightarrow f} = \frac{v_f \cdot \hat{e}_\perp \delta(\omega_f - \omega_i)}{\sum_j v_j \cdot \hat{e}_\perp \delta(\omega_j - \omega_i)} \quad (3)$$

where v_i and ω_i are the group velocity and frequency of the i -th phonon mode, \hat{e}_\perp is the wall normal vector pointing inwards the material and $\delta(\omega_j - \omega_i)$ is regularized using adaptive smearing [11]. Besides the steady-state, the code allows for the exploration of time evolution determined by boundary conditions. This is done by sampling the trajectories on a time grid on top of the spatial grid, in such a way that the contribution from a trajectory path inside a computational box to deviational energy (e^d) and heat flux (j) grid point is:

$$e^d(k, i) = \frac{1}{V_k} \sigma \varepsilon_d (t_f - t_0) [\Theta(t - t_i) - \Theta(t - t_{i+1})] \quad (4)$$

$$j(k, i) = \frac{1}{V_k} v \sigma \varepsilon_d (t_f - t_0) [\Theta(t - t_i) - \Theta(t - t_{i+1})] \quad (5)$$

where k is the computational box id, V_k is the volume of the k -th box, σ is the particle sign, ε_d is the deviational power carried per particle, v is the particle velocity and $(t_f - t_0) [\Theta(t - t_i) - \Theta(t - t_{i+1})]$ represents the interval between t_0 and t_f that belongs to the i -th point of the time grid, with Θ representing the Heaviside function. Such contribution is computed each time a particle changes its state or its spatial bin. Finally, by integrating Eqs. (4)-(5) one can obtain the evolution of temperature $T(k, t_i)$ and heat flux $J(k, t_i)$:

$$T(k, t_i) = T_{\text{ref}} + \frac{1}{C_v(T_{\text{ref}})} \sum_{l=0}^i e^d(k, l) \quad (6)$$

$$J(k, t_i) = \sum_{l=0}^i j(k, l) \quad (7)$$

where T_{ref} is the reference temperature and $C_v(T_{\text{ref}})$ is the volumetric heat capacity at T_{ref} .

3.2.1. A note on extended systems with applied gradients

For extended systems where no isothermal boundaries are present, e.g. an infinitely long nanoribbon with an applied thermal gradient, particles cannot exit the structure. It is therefore necessary to introduce an alternative way to collect them. For this purpose, and taking into account

that transient to steady-state is normally not of interest for those cases, we implemented a modified version of the algorithm originally proposed by Randrianalisoa *et al.* [25, 26] and adapted to such cases by Péraud *et al.* [17]. We now list our modifications to the algorithm, with respect to the finite systems described in Appendix D, for dealing with extended systems under applied gradients:

1. Generate particles from a gradient (source) generator, evolve them until they scatter (intrinsically or at borders or interfaces) and compute their contribution to steady-state.
2. Calculate the net number of particles that intrinsically scatter $N_j = \sum_i^{N_{\text{intrinsic}}} \sigma [r \in j]$ at each computational box and delete those particles.
3. Generate $|N_j|$ particles with sign $\sigma = \text{sgn}(N_j)$ from the postscattering distribution $\frac{C_{k'}(j)/\tau_{k'}(j)}{\sum_i C_i(j)/\tau_k(j)}$.
4. If the number of particles is 0, no new particles are introduced or the properties have converged, end the simulation; otherwise repeat step 1.

It is noteworthy that the cancellation scheme in step 2 introduces a non-negligible error of second order with respect to the space mesh [17].

3.2.2. Interface model for stacked layered systems: localized diffuse mismatch model

The traditional diffuse mismatch model (DMM) implemented for the treatment of interface scattering in `steady_montecarlo1d` is a purely elastic model, allowing the coupling between modes at each side of the interface with energy conservation as the sole requirement. Despite this crude approach, the DMM has been proven to qualitatively describe the interface thermal resistance (ITR) for several interfaces of bulk 3D materials such as Si/Ge [12]. However, for systems comprised of stacked layers, such as the interface between graphene and encapsulated graphene [27], energy matching as the single condition for transmission is no longer a valid assumption. Under such conditions, well localized modes in unconnected layers—e.g.: encasing hBN layers vs. the bare monolayer at the graphene/encapsulated-graphene interface—would be predicted to be coupled, which is quite unrealistic and would lead to too low (or even negligible or negative) ITR values (see Fig. 2) [27]. Consequently, we developed the localized DMM (LDMM) to account for mode localization at layers. To that end, we define the localization vector at the I -th layer for a given mode ($\mathcal{L}_{I,\lambda}^A$) as:

$$\mathcal{L}_{I,\lambda}^A = \frac{\sum_j^N \sum_\alpha^{x,y} |\zeta_{\lambda,\alpha,j}|^2 [j \in I]}{\sum_j^N \sum_\alpha^{x,y} |\zeta_{\lambda,\alpha,j}|^2} \quad (8)$$

where I is the layer index of A side, λ is the phonon mode index, j is the atomic index, α is the cartesian axis and $\zeta_{\lambda,\alpha,j}$ is the eigenvector. Therefore, when calculating the

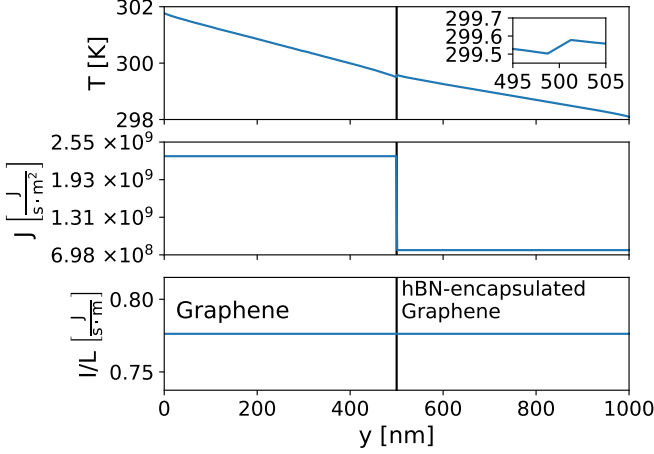


Figure 2: Thermal profile, flux and heat intensity per unit of length in graphene/hBN-encapsulated graphene obtained using the RTA and the traditional DMM to model interface scattering. Inset: Zoom of thermal profile at the interface.

coupling strength we multiply the classical DMM expression by the coupling factor $\mathcal{C}_{\lambda,\lambda'}^{A,B}$:

$$\mathcal{C}_{\lambda,\lambda'}^{A,B} = 1 - \text{JSD}(\mathcal{L}_{\lambda}^A || \mathcal{L}_{\lambda'}^B) \quad (9)$$

where $\text{JSD}(\mathcal{L}_{\lambda}^A || \mathcal{L}_{\lambda'}^B) \in [0, 1]$ is the Jensen-Shannon divergence between localization functions. Therefore, $\mathcal{C}_{\lambda,\lambda'}^{A,B}$ is one for perfectly matching localization and zero for modes fully localized at different layers. As the Jensen-Shannon divergence requires both vectors to be of same length, for different materials the localization vectors are modified in such a way that connected layers remain untouched and paired while the remaining unconnected layers have their values summed up and added at the back of the localization vector; we provide an example for reference:

$$\mathcal{L}_{\lambda}^C = \begin{pmatrix} \mathcal{L}_{\lambda,i}^C \\ \mathcal{L}_{\lambda,j}^C \\ \sum_k \mathcal{L}_{\lambda,k}^C \end{pmatrix}, \quad \mathcal{L}_{\lambda'}^D = \begin{pmatrix} \mathcal{L}_{\lambda',\alpha}^D \\ \mathcal{L}_{\lambda',\beta}^D \\ \sum_{\mu} \mathcal{L}_{\lambda',k}^D \end{pmatrix} \quad (10)$$

In this example, layers i and j of C are connected to the α and β layers on the D side, and k and μ denote all unconnected layers on each side or a zero term if no additional layers exist. In Fig 3 we show results for the same case studied in Fig. 2 but using the LDMM, enabling us to obtain a non-negligible ITR as expected in this kind of system [27]. It should be noted that, despite the improvement in the results, the model is still incapable of describing the thermal rectification predicted in such systems [27, 28] because of the intrinsic symmetry of the DMM and the Jensen-Shannon divergence used to model the interface scattering.

3.3. Beyond RTA Monte Carlo

Given the RTA's failure to describe the thermal properties of 2DMs [20, 21], we implemented in `beRTAMC2D`

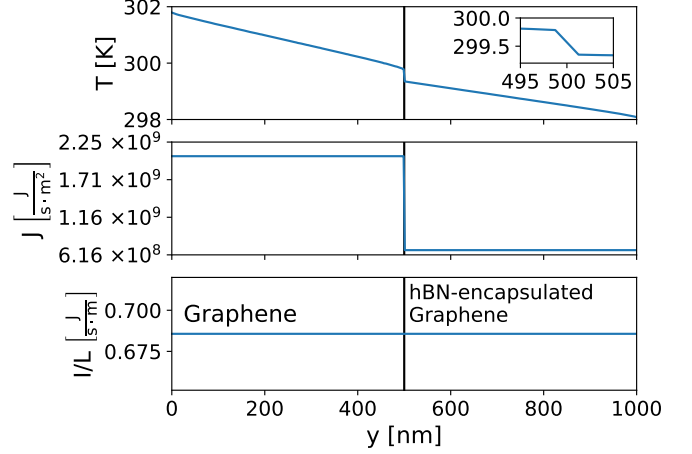


Figure 3: Thermal profile, flux and heat intensity per unit of length in graphene/hBN-encapsulated graphene obtained using the RTA and the LDMM to model interface scattering. Inset: Zoom of thermal profile at the interface

(see Appendix B.4) a linearized ab initio phonon-low variance deviational simulation Monte Carlo (LAIP-LVDSMC) [22] simulator to overcome such limitation. This LAIP-LVDSMC algorithm, henceforth referred to as *beyond RTA* (bRTA), solves the deviational energy linearized PBTE:

$$\frac{\partial n_i^d}{\partial t} + v_i \cdot \nabla_r n_i^d + \frac{\partial n_i^0}{\partial T} v_i \cdot \nabla_r T = \sum_j B_{ij} n_j^d \quad (11)$$

where n_i^d is the deviational energy distribution, n_i^0 is $\hbar\omega_i f_i^0 = \hbar\omega_i / (\exp(\hbar\omega_i/k_B T) - 1)$ and B_{ij} is the linearized scattering operator comprising three-phonon and isotopic (mass disorder) scattering terms:

$$B_{ij} = \sum_{sml} P_{s+m \rightarrow l}^{3ph} \left[\frac{\omega_s}{\omega_m} (f_l^0 - f_s^0) \delta_{is} \delta_{jm} + \frac{\omega_s}{\omega_l} (f_s^0 + f_m^0 + 1) \delta_{is} \delta_{jl} + (f_l^0 - f_m^0) \delta_{is} \delta_{ji} \right] + \frac{1}{2} \sum_{sml} P_{s \rightarrow n+l}^{3ph} \left[\frac{\omega_s}{\omega_m} (f_l^0 - f_s^0) \delta_{is} \delta_{jm} + \frac{\omega_s}{\omega_l} (f_m^0 - f_s^0) \delta_{is} \delta_{jl} - (f_l^0 + f_m^0 + 1) \delta_{is} \delta_{ji} \right] + \sum_{sm} P_{s \rightarrow m}^{iso} \left[\frac{\omega_s}{\omega_m} \delta_{is} \delta_{jm} - \delta_{is} \delta_{ji} \right] \quad (12)$$

where $P_{s+m \rightarrow l}^{3ph}$ and $P_{s \rightarrow m+l}^{3ph}$ are the intrinsic transition probabilities for three-phonon absorption and emission processes, derived from perturbation theory [6, 11] and $P_{s \rightarrow m}^{iso}$ is the intrinsic isotopic transition calculated using Tamura's model [29]. The latter was not included in Landon's original algorithm. The PBTE is then solved using a Monte Carlo scheme with each step split in two parts: advection, in which we introduce, evolve and scatter particles at boundaries (see Appendix E for more details) and

scattering within the material, in which the distribution evolves according to

$$n(t + \Delta t) = P(\Delta t)n(t) = e^{B\Delta t}n(t) \quad (13)$$

where the propagator $P(\Delta t)$ is a non-Markovian transition matrix, as it has negative or higher than unity elements [30], which makes its direct implementation difficult. A more implementation-friendly form can be obtained by using the power series:

$$n_i(t + \Delta t) = \sum_j \frac{P_{ij}(\Delta t)}{\mathcal{P}_j} \left(\sum_{n=0}^{\infty} \left(2 \frac{\mathcal{P}_j^-}{\mathcal{P}_j} \right)^n \right) n_j^d(t) \quad (14)$$

where $\mathcal{P}_j = \sum_k^{N_{\text{states}}} |P_{kj}|$ and $\mathcal{P}_j^- = \sum_k^{N_{\text{states}}} |P_{kj}| [P_{kj} < 0]$. The recursive Eq. (14) can be implemented stochastically for a particle in state j with sign σ through the following strategy:

1. Sample a random number R in $[0, 1)$, and find the lower bound f of $\sum_k |P_{kj}(\Delta t)| / \mathcal{P}_j$ for R .
2. Set the new sign to $\sigma' = \text{sgn}(P_{fj}\sigma)$.
3. If $\sigma' \neq \sigma$, generate two particles with state j and time t .

Finally, the deviational energy density ρ^d and the heat flux J are obtained from the distribution in the i -th computational box as:

$$\rho^d(i) = \frac{\sum_j^{N_{\text{particles}}} \varepsilon_d \sigma_j [r_j \in i\text{-th box}]}{V_{i,\text{box}}} \quad (15)$$

$$J(i) = \frac{\sum_j^{N_{\text{particles}}} v_j \varepsilon_d \sigma_j [r_j \in i\text{-th box}]}{V_{i,\text{box}}}, \quad (16)$$

where ε_d is the deviational energy per particle and r_j is the position of the j -th particle.

3.3.1. B_{ij} calculation and enforcement of conservation laws

As noted by Landon *et al.*, it is important for B_{ij} to respect crystal symmetries and microscopic reversibility [22]. The original `almaBTE` routines for calculating scattering amplitudes lead to violations of those constraints because the smearing method implemented there does not enforce the symmetry between emission and absorption processes [11, 31].

To enforce symmetry, matrix elements are built from a single representative of each equivalence class in the quotient group of q points using a new symmetric adaptive smearing scheme for energy conservation

$$\sigma_{ijk} = a \sqrt{\sigma_i^2 + \sigma_j^2 + \sigma_k^2} \quad (17)$$

$$\sigma_i = \frac{1}{\sqrt{12}} \|\{G_{\mu\alpha}^T \cdot N_{\mu\mu}^{-1}\}^T \cdot (v_i)_\alpha\| \quad (18)$$

where i , j and k are the phonon modes taking part in the three-phonon process, μ indicates a reciprocal-space

lattice vector, α indicates a Cartesian axis, $G_{\mu\alpha}$ is the reciprocal lattice basis matrix, $N_{\mu\mu}$ is a diagonal matrix whose elements are the size of the q -point grid, and a is a broadening factor. The theoretically optimal value of a is 1, but it can often be decreased with significant gains in performance and little degradation in accuracy.

Next, those matrix elements are expanded using crystal symmetry and microscopic time reversibility and averaged to eliminate possible asymmetries. This lookup, together with matrix building, is parallelized via MPI and OpenTBB, with stable summations following Neumaier's algorithm for matrix collapse and gathering [32].

Finally, it must be noted that B_{ij} requires a rather strict conservation of energy, which is violated by the broadening scheme. Therefore, we add a correction extracted from a Lagrange-multiplier approach [22] to our matrix to enforce it. On top of that, Landon *et al.* also discussed the necessity of including a momentum correction to make normal processes conserve the momentum. However, we found that including such correction was unnecessary and, in fact, results in spurious effects such as nonnegligible fluxes in directions perpendicular to the thermal gradient for homogeneous bulk systems.

3.3.2. Efficient propagator calculation

The scattering algorithm requires the explicit calculation of the propagator matrix $P(\Delta t) = e^{B\Delta t}$ [see Eq. (14)]. Although the matrix exponential is a well defined mathematical operation given by:

$$e^{B\Delta t} = \sum_{n=0}^{\infty} \frac{\Delta t^n}{n!} B^n, \quad (19)$$

its practical computation is cumbersome and still a topic under active research, with lots of methods available [33]. One of the most common approaches to computing e^A is the scaling-and-squaring method [34, 35], also chosen by Landon in his original work [30]. The method is based on squaring the matrix to reduce its norm, then computing the exponential using a Padé approximant and undoing the squaring, with an overall computational cost of at best $20N^3$ operations for dense matrices of size N [35]. For reference, the B -matrix of the prototypical 2DM, graphene, contains approximately 1.5×10^9 elements when a $80 \times 80 \times 1$ grid is used, so the scaling and squaring method is not suited for our problem.

In contrast, Krylov subspace methods are especially suited for big matrices, where the action of the exponential matrix (e^A) on vector (b) can be approximated using much more smaller matrices. The Krylov subspace ($\mathcal{K}_n(A, b)$) of order n is a vector subspace spanned by $\{b, Ab, A^2b, \dots, A^{n-1}b\}$, an orthonormal basis (S_n) of which can be build via Arnoldi iteration [36]. The problem can be then recast in terms of $\mathcal{K}_n(A, b)$ as [33, 37]:

$$e^A b \approx \|b\| S_n e^{H_n} e_1 \quad (20)$$

where H_n is the projection of A on the basis S_n (of size $n \times n$) and e_1 is the first column of the identity matrix. The Krylov subspace size and therefore the dimensions of H_n may be truncated down to a desired precision via the error bound $\|e^A b - \|b\| S_n e^{H_n} e_1\| \leq 2\|b\| \frac{\|A\|^n e^{\|A\|}}{n!}$ [38]. In fact, small values of n tend to give good approximations and enable a calculation of the small $n \times n$ sized e^{H_n} -matrix efficiently through the scaling and squaring method. Despite its efficiency and suitability for our case, the Krylov subspace method is limited to the calculation of arbitrary matrix-vector products $e^A b$, not of e^A itself. Nevertheless, one can easily recover each column of e^A by using canonical basis vectors as b -vectors. This way of calculating e^A has the added advantage of being straightforward to parallelize, as each column can be calculated independently.

3.3.3. Linear interpolation of the propagator for systems with multiple reference temperatures

From Eq. (12) it becomes clear that different reference temperatures would require different propagators. This is not problematic per se, but the fact that each propagator occupies a big amount of RAM can be a problem for simulations with variable reference temperatures [17]. To relieve the memory burden for such simulations we use on-the-fly linear interpolation of $P(\Delta t)$ between pairs of temperatures, thus requiring memory storage only for a few reference propagators. Linear interpolation was chosen because it ensures energy conservation at the interpolated temperatures. We tested the performance of these linear interpolants against the corresponding exact propagators by calculating the error per element between the phosphorene propagator at 305 K and the interpolated result using 300 K and 310 K as knots. We also did the same for 320 K using 300 K and 340 K as knots. In both cases, we obtained an error per element in the order of 10^{-6} .

4. Code Validation

As previously mentioned, 2DMs are being extensively studied as possible substitutes of silicon in MOSFET [39, 40, 41]. Amid all candidates to succeed silicon, the monolayer, also known as phosphorene, and few-layer black phosphorous (bP) have attracted lots of attention due to its electronic properties, such as its high mobility when compared to other candidates like transition metal dichalcogenides [42]. Indeed, is it possible to find several examples of fully functional MOSFETS based on few-layer bP [43, 44, 42]. The work of Wu *et al.* is of interest, presenting high-performance MOSFETs with reconfigurable polarities [45]. Furthermore, phosphorene has been proposed to be an important actor in the survival of Moore’s law down to atomic sizes [46] thus increasing the importance of controlling heat transport for phosphorene at the device level.

Therefore, in this section we present phosphorene-based test cases. To that end, we have used first-principles

Table 1: Calculated κ for phosphorene at 300 K along the armchair (AC) and zigzag (ZZ) directions using the RTA.

	AC [$\frac{\text{W}}{\text{m}\cdot\text{K}}$]	ZZ [$\frac{\text{W}}{\text{m}\cdot\text{K}}$]
κ_{almaBTE}	20.7	57.8
$\kappa_{\text{RTA}}^{\text{MC}}$	20.3±0.1	56.2±0.2

data—i.e.: atomic positions and interatomic force constants of second and third order—of Ref. 47 to obtain phonon properties (frequencies, eigenvectors, lifetimes, group velocities, etc.) alongside with the propagator. Second-order interatomic force constants were renormalized to enforce crystal symmetry, translational invariance and rotational invariance necessary for a proper description of quadratic acoustic bands [48], the broadening parameter was fixed to 1 for energy conservation and the layer thickness was set to 0.533 nm [49]. The phonon properties and the propagator were calculated on a Γ -centered q -mesh of $50 \times 50 \times 1$ points, for which thermal bulk conductivity is found to be converged—with less than a 5% change with respect to a higher quality mesh of $100 \times 100 \times 1$ points—at 300 K. The propagator for the bRTA calculations was calculated using a time step of 0.25 ps.

4.1. RTA code validation

To validate the RTA code, we simulated an infinitely large piece of phosphorene with an applied thermal gradient represented as a source generator (see Sec. 3.2.1 and Appendix D) as depicted in Fig. 4.

$\kappa_{\text{AC,RTA}}^{\text{MC}}$ and $\kappa_{\text{ZZ,RTA}}^{\text{MC}}$ were calculated via Fourier’s law from fluxes ($J_h = -\kappa_l \nabla_r T$). The results are quite close to the ones obtained using `almaBTE`’s bulk thermal conductivity calculator, `kappa_Tsweep` (see Table 1); with the differences being less than the typical experimental error of 5% for thermal conductivities [50].

We conducted an additional test of this RTA algorithm by comparing it to an RTA version of bRTA (see Appendix F). To do so we simulated an infinite nanoribbon (NR) in the AC direction with an applied gradient of 0.2 K nm^{-1} along the NR. The heat flux profiles from both methods, plotted in Fig. 5, are in excellent agreement.

4.2. Beyond RTA: B-matrix validation

To validate our B_{ij} construction algorithm we used the resulting matrix to obtain the lattice thermal conductivity

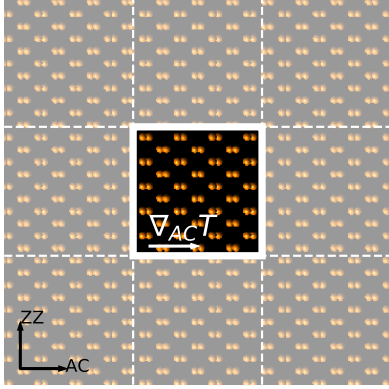


Figure 4: Sketch of the simulation setup for perfect phosphorene with a thermal gradient applied in the AC direction. Replicas illustrating the periodic boundary conditions are depicted as off-color boxes.

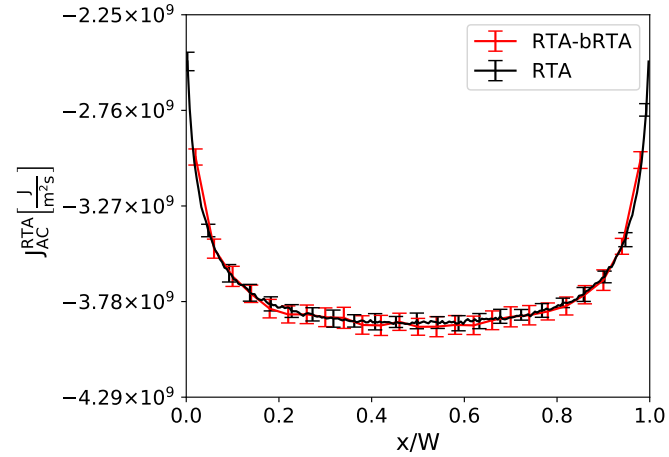


Figure 5: Comparison of RTA (black) and RTA-bRTA (red) heat flux in AC direction as function of normalized position for a phosphorene nanoribbon of 400 nm of width with $\nabla_{AC}T = 0.2 \text{ K nm}^{-1}$.

Table 2: Calculated κ for phosphorene at 300 K for armchair (AC) and zigzag (ZZ) directions. Other theoretical results are provided for comparison.

	AC [$\frac{\text{W}}{\text{m}\cdot\text{K}}$]	ZZ [$\frac{\text{W}}{\text{m}\cdot\text{K}}$]
κ_{almaBTE}	27.501	82.878
κ_{B}	27.499	82.860
Ref. 51 [†]	23.9	82.1
Ref. 52 [†]	35.5	108.3
Ref. 47	22.0	63.2

[†] These results are rescaled to take into account differences in assumed thickness.

(κ_l) by iteratively solving the linear system:

$$\left(\frac{\partial n_i^0}{\partial T} v_i \cdot \nabla_r T \right)_i = \sum_j B_{ij} n_j^d \quad (21)$$

using the RTA solution ($n_j^{d,RTA} = \frac{1}{B_{jj}} \frac{\partial n_j^0}{\partial T} v_j \cdot \nabla_r T$) as an initial guess, and we then compared the results against `almaBTE`'s `kappa_Tsweep` for the case of phosphorene (see Table 2). The agreement between both methods and the fact that they are in line with other theoretical calculations provide support to our methodology.

4.3. Beyond RTA: Propagator and bRTA validation

To validate $P(\Delta t)$ together with the rest of the bRTA implementation, we simulated an infinitely large piece of phosphorene with an applied thermal gradient represented as a source generator [see Eq. (D.2)], as shown in Fig. 4.

The MC heat fluxes for the infinite phosphorene under thermal gradients along the ZZ and AC directions are plotted in Fig. 6. κ_{AC}^{MC} and κ_{ZZ}^{MC} are calculated via Fourier's law ($J_h = -\kappa_l \nabla_r T$) to be $27.4 \pm 0.2 \text{ W}/(\text{m} \cdot \text{K})$ and $82.8 \pm 0.5 \text{ W}/(\text{m} \cdot \text{K})$ respectively. Those results show an excellent agreement between iterative and MC solutions, thus validating our bRTA implementation.

5. Results

5.1. Phosphorene devices

In this section we present thermal transport results for different phosphorene-based configurations/devices using the simulators developed in previous sections.

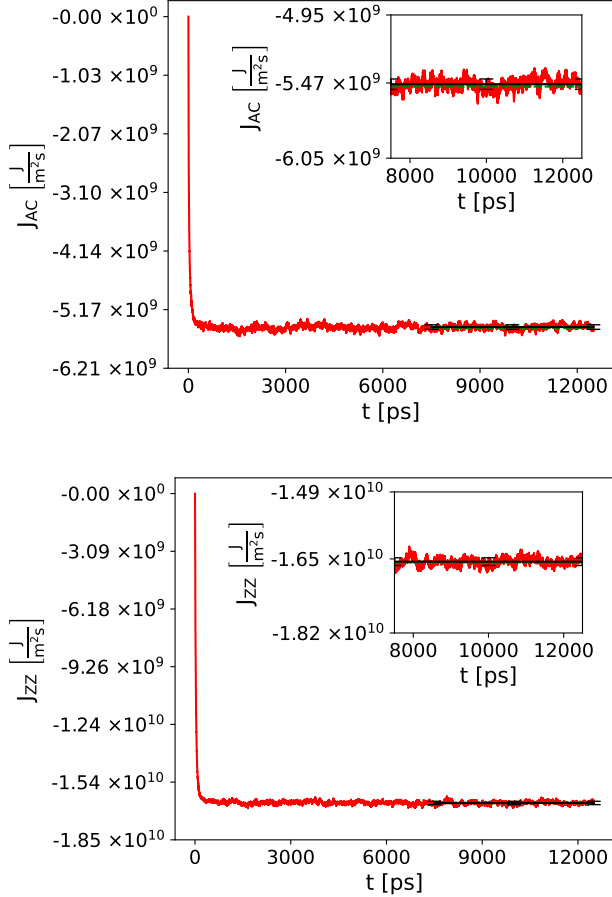


Figure 6: bRTA heat flux as function of simulation time (red) and average steady-state flux (black) in AC (top) and ZZ (bottom) for infinitely large phosphorene at 300 K under an applied thermal gradient of 0.2 K nm^{-1} in the transport direction. The iterative result calculated via Fourier's law with κ_{almabTE} is given in both cases for comparison (dashed green). Inset: zoomed view of the steady-state region used to compute the mean flux.

5.1.1. Nanoribbons

Among the simplest 2D-based systems used in devices are nanoribbons [40, 41]. We have calculated the heat transport in infinite phosphorene AC nanoribbons under the effect of a thermal gradient of 0.2 K nm^{-1} . The results of the normalized heat flux relative to the bulk value, together with an RTA rescaled version for three different widths are shown in Fig. 7.

As expected, boundary scattering increases and becomes dominant over other mechanisms in thinner nanoribbons. This is clearly seen in the reduction of heat flux with decreasing width and the fact that the difference between the RTA and beyond-RTA methods vanishes for smaller ribbons (see the 4 nm case in Fig. 7a), since boundary scattering is not dependent on the approach used to describe intrinsic anharmonic and isotopic scattering. Consequently, for wide nanoribbons in which anharmonic and isotopic scattering are dominant it should be possible to obtain a good approximation to bRTA results by simply using a $\kappa_{\text{almabTE}}/\kappa_{\text{RTA}}$ -rescaled RTA (see Fig. 7b). Indeed, the main differences between this estimate and bRTA for the 400 nm-ribbon are in the regions near the boundaries, in which the bRTA flux is lower than the rescaled version. Although also visible in other cases, this is more pronounced in the wider nanoribbon.

In view of the above, the RTA clearly overestimates the momentum destruction due to intrinsic scattering leading to more diffusive flux profiles when compared to bRTA results. The latter yields more Poiseuille-like profiles, with stronger hydrodynamic features, by properly capturing the coupling between phonon modes [20, 53].

To further explore those hydrodynamic signatures, we fitted our nanoribbon results to a mesoscopic equation based on Sellitto *et al.*'s work [54]:

$$J(x) = -\kappa \left\{ 1 - \left[\frac{1}{1 + C \tanh\left(\frac{W}{2\ell}\right)} \right] \frac{\cosh\left(\frac{x}{\ell}\right)}{\cosh\left(\frac{W}{2\ell}\right)} \right\} \nabla T \quad (22)$$

where W is the nanoribbon width, x is the distance from the center of the nanoribbon, ℓ is the non-local length [55] and C is related to wall properties, taking a value of 2 in our case because we have assumed completely diffusive walls.

In Figs. 8 and 9 the fits of our RTA and bRTA simulator results to hydrodynamic mesoscopic equation for nanoribbons are shown; in both we obtain a set of parameters that accurately match the simulation results. The agreement afforded by the beyond-RTA method is, however, slightly better.

As for the fitted parameters, we can observe a relative fast convergence of thermal conductivity towards bulk values as the nanoribbon gets wider and boundary scattering effects become negligible in the middle of the strip (see

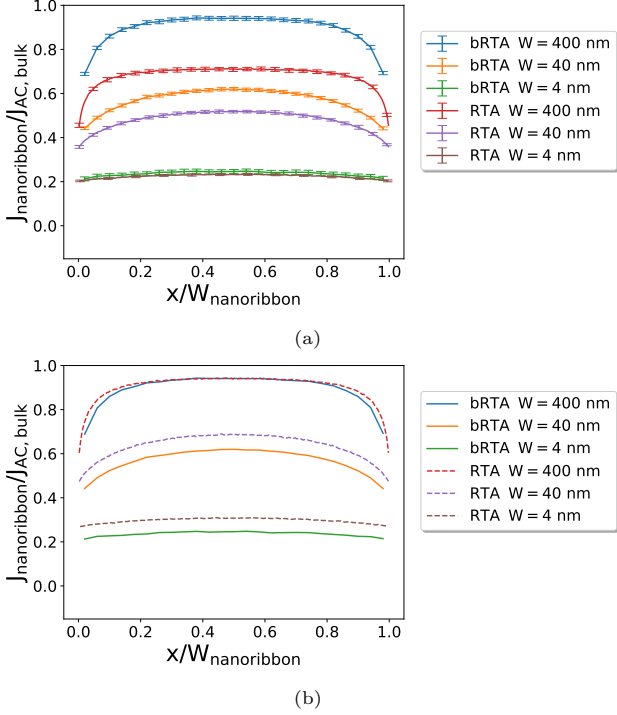


Figure 7: Top: RTA and bRTA bulk-normalized heat flux in the AC direction as a function of the normalized position for a phosphorene nanoribbon with $\nabla_{AC}T = 0.2 \text{ K nm}^{-1}$. Bottom: Comparison of bulk-normalized bRTA and $\kappa_{\text{almaBTE}}/\kappa_{\text{RTA}}$ -rescaled RTA heat fluxes.

Fig. 10). The value of the non-local length (ℓ) rises towards a converged value as the ribbon becomes wider (see Fig. 11), in agreement with what is expected from a microscopic description of the value [55]. The observed differences between RTA and the higher beyond-RTA ℓ values, especially for larger widths, can be easily interpreted by keeping in mind that in RTA all scattering processes are deemed as resistive and introduce artifactual modifications of the heat flux. It should be noted that the theoretical formulas used to obtain the $\ell^{\text{RTA,iso}}$ values are derived under the assumption of isotropy and are therefore expected to be useful only as approximations in our case. For reference, the results for ZZ-nanoribbons are also given in Appendix G.

Finally, we have also obtained κ_{nano} for nanoribbons of several widths with both types of edges using the methodology for solving the PBTE in systems with edges described in Sec. 3.1 (see Fig. 12). For consistency check, we compared the effective flux obtained via Fourier using κ_{nano} with the flux average over width obtained from Monte Carlo simulators, obtaining, as can be seen in Fig. 13, an excellent match between both methods.

5.1.2. RTA, bRTA and Fourier heat equation comparison

Taking into account that operational frequencies of microprocessors are limited to the GHz by cooling constraints [46, 56], it is of interest to be able to study heating dynamics at short times. As an example of capabilities to

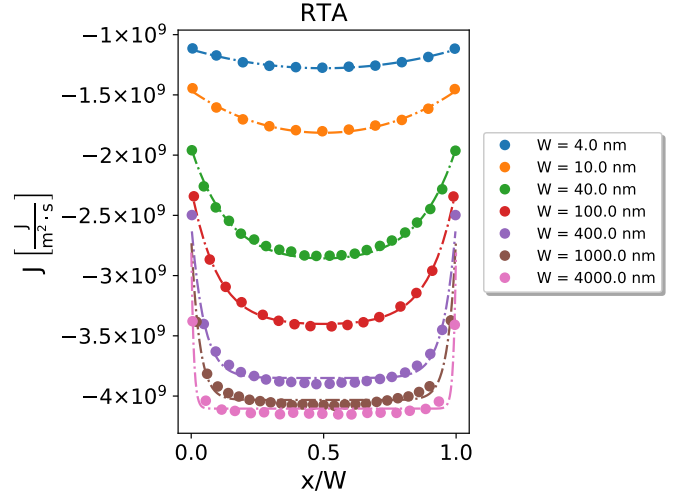


Figure 8: Fitting to Eq. 22 (lines) of RTA-MC calculated heat flux (points) as a function of normalized position for phosphorene AC nanoribbons of different widths under the effect of $\nabla_{AC}T = 0.2 \text{ K nm}^{-1}$.

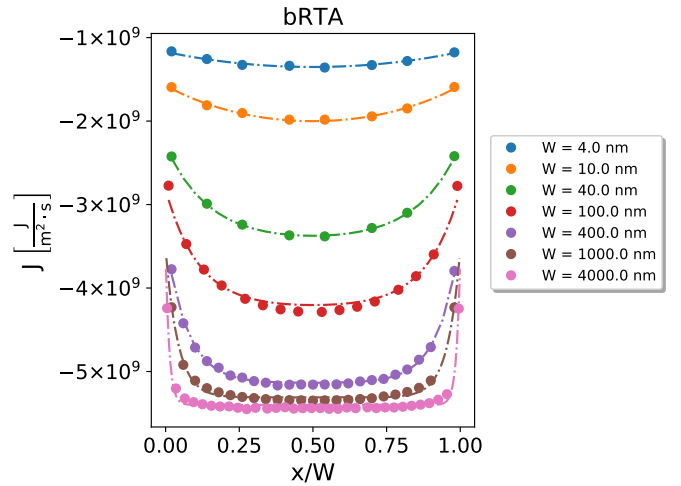


Figure 9: Fitting to Eq. 22 formula (lines) of bRTA calculated heat flux (points) as a function of normalized position for phosphorene AC nanoribbons of different widths under the effect of $\nabla_{AC}T = 0.2 \text{ K nm}^{-1}$.

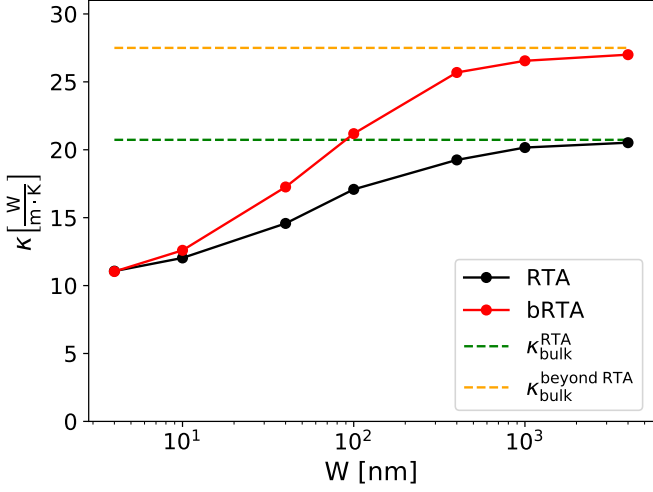


Figure 10: Fitted thermal conductivity as a function of AC nanoribbon width for RTA (black) and bRTA (red) MC calculations. RTA (green) and beyond RTA (orange) bulk values are given for reference.

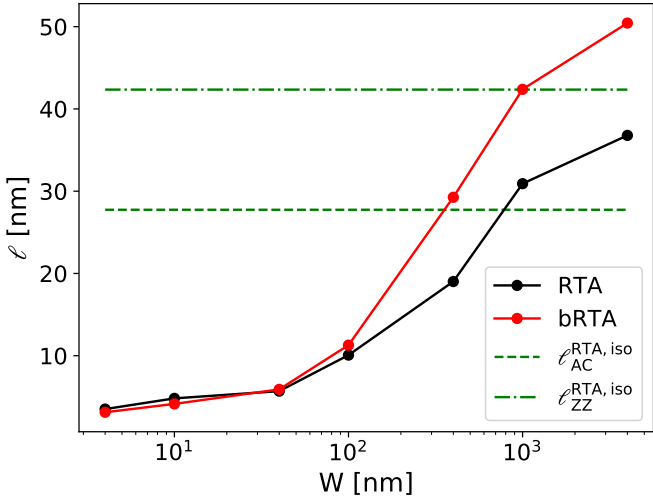


Figure 11: Fitted non-local distance ℓ as a function of AC nanoribbon width for RTA (black) and bRTA (red) MC calculations. RTA bulk values of ℓ calculated using Sendra et. al.'s formula [55] are given for reference (green).

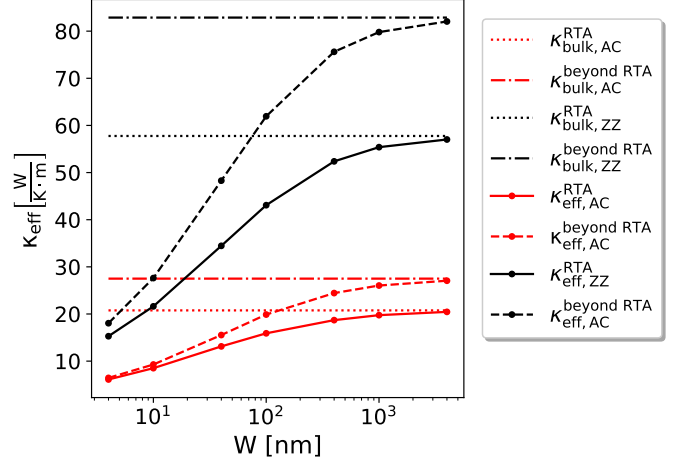


Figure 12: Effective thermal conductivity for AC and ZZ nanoribbons of different widths at 300 K obtained through the direct (RTA) and iterative (beyond the RTA) solution of the linerized-PBTE. Bulk values are provided as reference.

simulate short heating dynamics, we have studied the temperature time evolution for a piece of phosphorene initially at 300 K with periodic boundary conditions in the AC direction and sandwiched between two isothermal reservoirs, at 300 K and 302 K, in the ZZ direction (see Fig. 14).

Fig. 15 shows the RTA, bRTA and Fourier ($\frac{\partial T}{\partial t} = \alpha \nabla^2 T$, where α is the thermal diffusivity: $\alpha = \kappa/C_v$) heat profiles at two different times. The difference between the Fourier heat equation and BTE results at short times is a well known shortcoming of the former [57, 58]. Regarding PBTE solutions, bRTA and RTA results clearly differ at this instance. The bRTA shows a faster heating, which is not surprising since RTA scattering completely randomizes momentum, thus dampening the fluxes and leading to a lower thermal conductivity.

In Fig. 17 we plot the spectral decomposition of the contributions to the deviational temperature at the middle and near the hot edge of the beam. In keeping with the fact that differences between the RTA and bRTA solutions are the largest in the middle of the bar (see Fig. 15), spectral decompositions of the deviational temperature deviate the most at the middle as opposed to the edges. They also vanish with time as both tend to the same temperature profile (see Figs. 17a-17d). Moreover, from the spectral decomposition it can also be seen that differences are more prominent at low frequencies, corresponding to phonons with longer intrinsic lifetimes (see Fig. 16), which indicates that the decay of such modes is clearly much more overestimated than for high-frequency ones. This explains the large disparity between the RTA and bRTA conductivities. It is therefore advisable to resort to the bRTA method for modeling fast/short heat dynamics, for example when studying heat dissipation in state-of-the-art electronic devices, as less sophisticated approximations fail to describe it accurately.

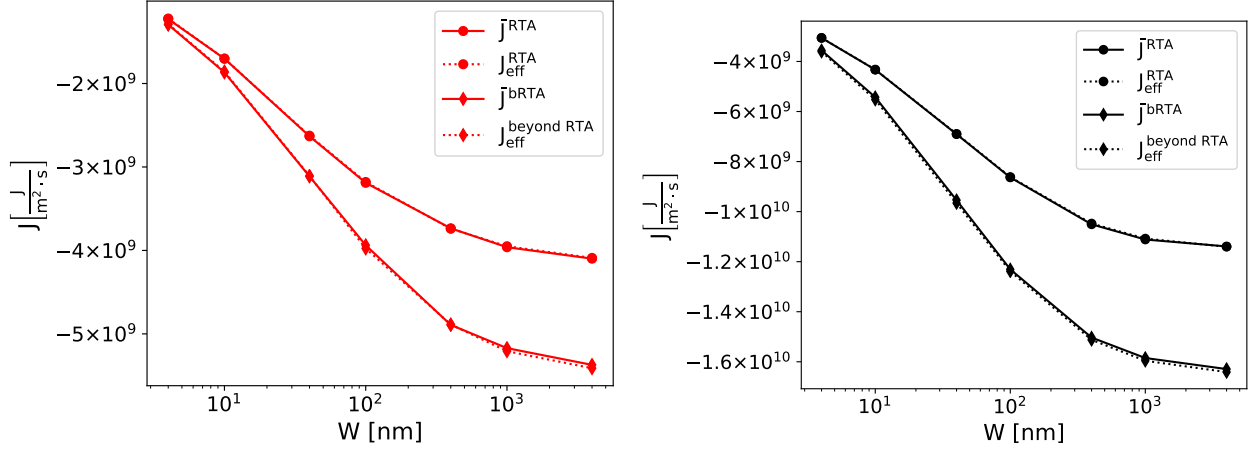


Figure 13: Comparison between effective RTA and beyond RTA heat fluxes for AC (left) and ZZ (right) nanoribbons and the respective Monte Carlo obtained fluxes for a 0.2 K nm^{-1} gradient in the unbound direction.

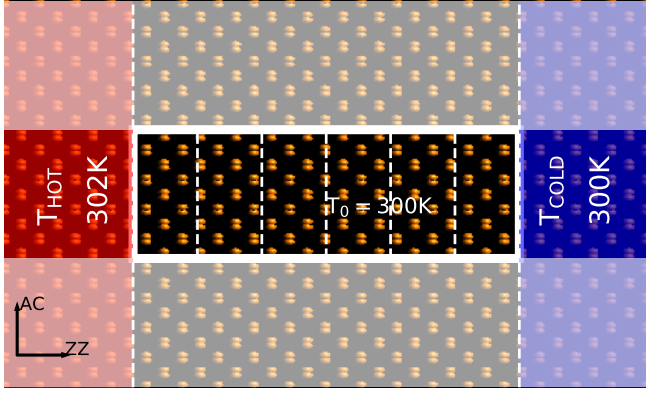


Figure 14: Sketch of phosphorene heating simulation in AC direction. Periodic boundary conditions are depicted with off-color boxes.

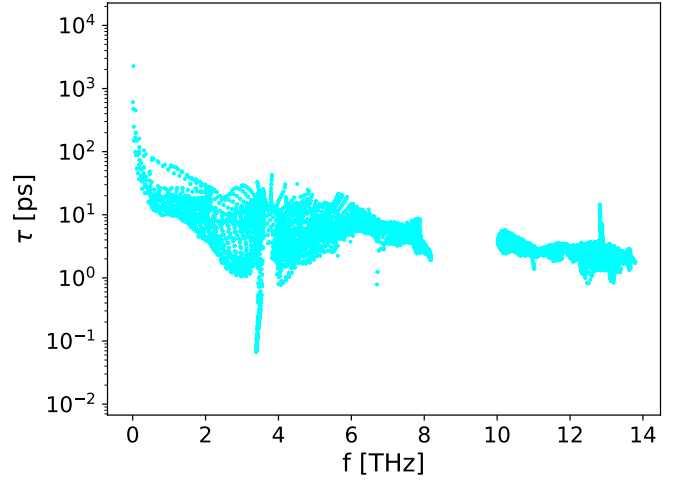


Figure 16: Bulk-phosphorene lifetimes as function of frequency at 300 K.

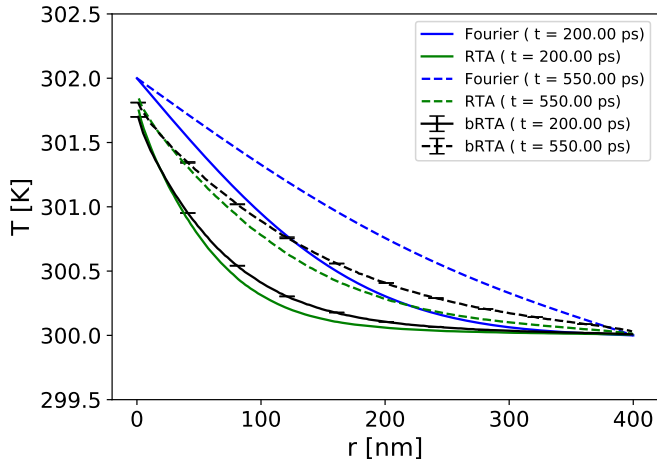


Figure 15: Temperature profiles obtained with the RTA (green), bRTA (black) and Fourier (blue) approaches as functions of position for an AC-phosphorene bar at 200 ps (solid) and 550 ps (dashed).

5.1.3. Finite device examples

As previously mentioned, being able to predict thermal transport in complex devices and geometries is of key importance. To this end, we show examples for more complex systems, either because they have geometrical elements which are difficult to model computationally, such as a wedge geometry (see Fig. 18), or because they present interesting elements from a simulator capability point of view such as more than two terminals, which is a common experimental setup.

Steady-state temperature profiles and heat fluxes for the wedge-like geometry within and beyond the RTA for two different configurations, depending on which terminal is put at 301 K (the one at the top or the one at the bottom) while the other is kept at the reference temperature of 300 K, can be seen at Figs. 19 and 20 respectively. Similar asymmetric devices are used as thermal rectifiers, but we cannot expect to detect rectification here because

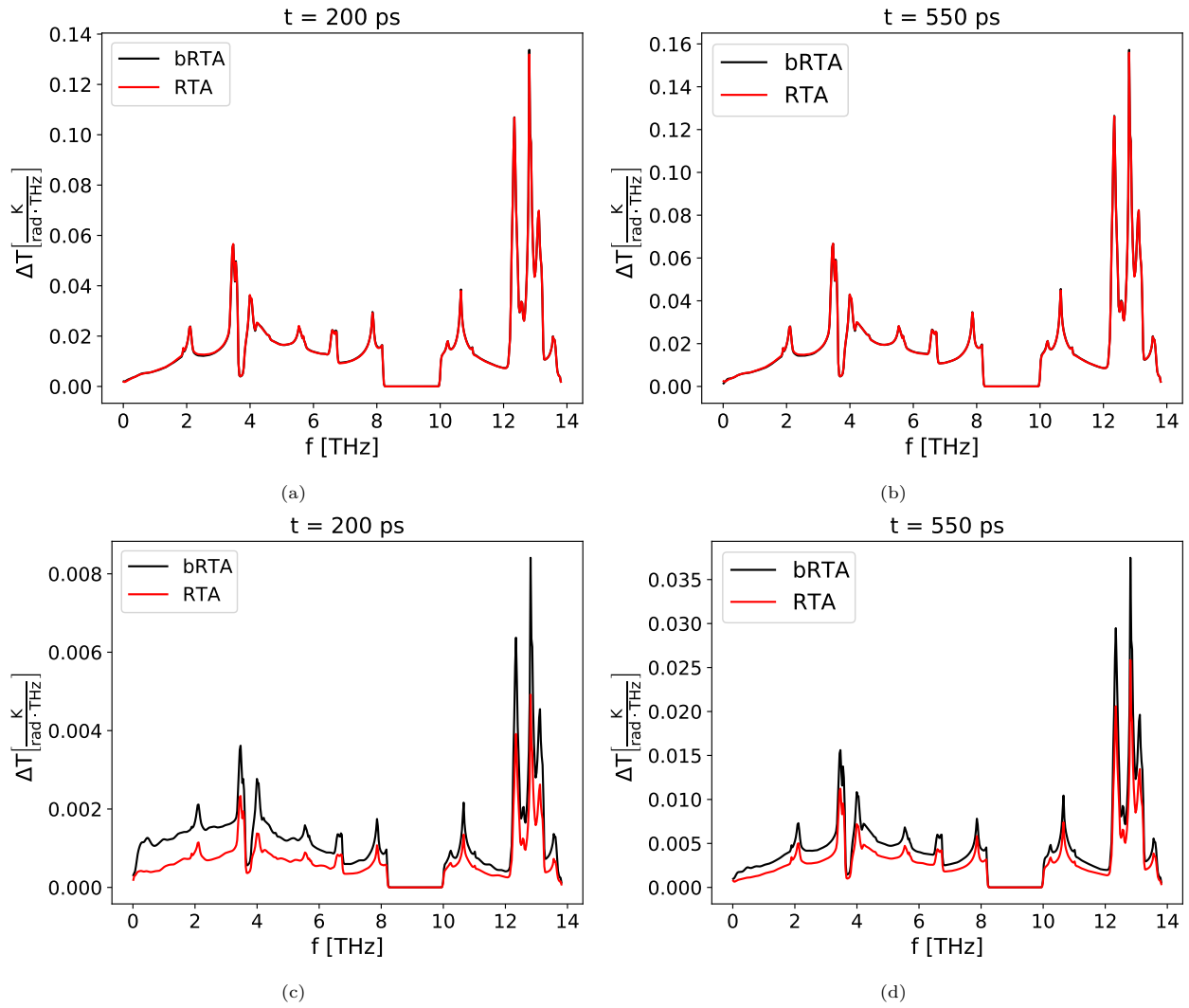


Figure 17: RTA (red) and bRTA (black) spectral decomposed temperature deviations for 400 nm ZZ-phosphorene bar at 15 nm (a and b) and 203 nm (c and d) from the hot edge, at times 200 ps and 550 ps.

this model is based on the bulk spectrum and therefore does not account for phenomena such as device-reservoir interactions or size-dependent vibrational spectra [59, 60]. Moreover, it should be noted that thermal differences used here are too small for any sign of thermal rectification to be significant over statistical noise [59], or to activate the rectification mechanism based on different temperature-dependent behavior [59, 61, 62]. Higher thermal differences are however unattainable with the current implementation as the error introduced by the linearization of the collision operator would be too high.

The heat fluxes and temperature profiles for the multiterminal structure (Fig. 21) are presented in Figs. 22 and 23, showing the capability of our simulator to properly account for several sources/drains (isothermal reservoirs). Indeed, for the bRTA case, there is even an additional population of phonons due to the initial conditions, as the initial temperature profile was set to the RTA estimate in order to accelerate its convergence to the steady-state.

5.2. Results: Example of material junction

Finally, to show the capability of our improved RTA simulator to describe devices with different materials, we present the temperature profile (Fig. 24) in a finite device structure composed by graphene on one half and h-BN encapsulated graphene on the other half (see Fig. 25). The first-principles data needed for this calculation were obtained from Ref. 63 in the case of graphene, where those properties had been calculated on a $80 \times 80 \times 1$ q -mesh with a broadening parameter of 1 and a conventional thickness of 0.345 nm [22]. Regarding h-BN encapsulated graphene, the required first-principles data were obtained using density functional theory using Perdew-Burke-Ernzerhof functional [64] plus the D3 [65, 66] correction to energy due to van der Waals interactions between layers as implemented in VASP [67, 68, 69] with a Γ -centered k -mesh of $7 \times 7 \times 1$ points for minimization, and using Phonopy [70] and thirdorder.py [11] with a supercell of $7 \times 7 \times 1$ to obtain second and third order interatomic force constants, respectively. The phonon properties of h-BN-encapsulated graphene were calculated using a $40 \times 40 \times 1$ Γ -centered q -mesh with a broadening parameter of 1 and setting the stack thickness to 1.001 nm [22, 71, 72].

6. Conclusions

In this work we have presented BTE-Barna, a software package that extends the almaBTE package to calculate the thermal properties of devices and systems based on 2D materials. We have showcased the new capabilities with an extensive set of tests and examples. For instance, the package was used to highlight the differences in the heat flux profile for the case of Poiseuille flow in a nanoribbon, for the case of RTA and beyond the RTA. Amid all new features the most relevant are:

1. The iterative solver has been extended to provide the effective conductivity for nanoribbons (and nanowires in the case of 3D materials).
2. The RTA Monte Carlo simulator was updated so that now it can address finite and/or periodic 2D systems under the effect of thermal gradients and isothermal reservoirs. Moreover, it now provides information for transient to steady-state for finite systems.
3. A beyond-RTA Monte Carlo simulator for 2D systems was implemented to provide an accurate description for those cases in which RTA fails.

This package is published as almaBTE's fork and is freely available to download at <https://github.com/sousaw/BTE-Barna>. Overall, we expect BTE-Barna to provide a new set of tools for design and prediction of thermal transport/management in 2D based devices and systems.

Acknowledgements

M.R.-M. and X.C. acknowledge financial support by Spain's Ministerio de Ciencia, Innovación y Universidades under Grant No. RTI2018-097876-B-C21 (MCI-U/AEI/FEDER, UE), and the EU Horizon2020 research and innovation program under grant GrapheneCore3 881603. M.R.-M. acknowledges financial support by the Ministerio de Educación, Cultura y Deporte programme of Formación de Profesorado Universitario under Grant No. FPU2016/02565 and Ministerio de Universidades under grant EST19/00655, as well as the kind hospitality of the Institute of Materials Chemistry, TU Wien.

Appendix A. Effective thermal conductivity in simple nanosystems: inputs, outputs and executable

The calculation of the effective thermal conductivity κ_{nano} for nanowires and nanoribbons at both the RTA and beyond RTA levels is implemented in the `kappa_Tsweep_nanos` executable. The calculation is performed as in `kappa_Tsweep` [12], but using $\tau_{\lambda}^{\text{nano}}$ in place of τ_{λ}^0 . Because of boundaries breaking crystal symmetry (i.e.: $S_{\lambda}^{\text{nano}}$ and consequently $\tau_{\lambda}^{\text{nano}}$ not possessing crystal symmetry), one needs to solve the linear system in the full Brillouin Zone; hence, `kappa_Tsweep_nanos` first recalculates and symmetrizes all bulk processes in the whole q -mesh, and if beyond RTA is required it solves the linear system using sparse matrices. The executable parameters are the same as for `kappa_Tsweep` but with an additional parameter to control the number of TBB threads in which the recalculation and symmetrization will take place.

`kappa_Tsweep_nanos input.xml Nthreads`

Regarding input files, it uses the same format as `kappa_Tsweep` but with some additions:

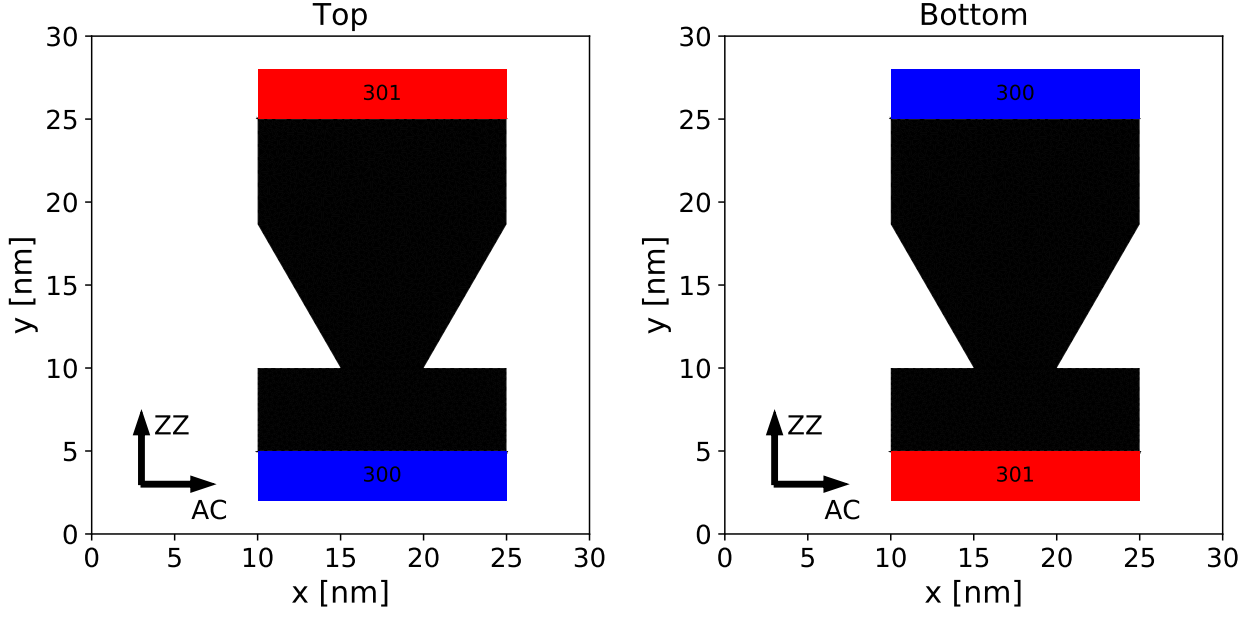


Figure 18: Phosphorene wedge-like geometry with hot reservoir at the top or at the bottom.

```
<system name="nanoribbon" L="500.0"/>
<AnharmonicIFC name="FORCE_CONSTANTS_3RD"
scalebroad="1.0"/>
```

1. system/name [string]: Indicates the type of nanosystem. Accepted values: `nanowires` and `nanoribbons`.
2. system/L [double,units(nm)]: limiting length of the system, radius for nanowires and width for nanoribbons.
3. AnharmonicIFC/name [string]: path to file containing third-order force constants. Only needed for beyond calculations.
4. AnharmonicIFC/scalebroad [double]: broadening parameter for adaptative smearing. Only needed for beyond-RTA calculations.

Finally `kappa_Tsweep_nanos` will produce a csv output file (`{h5filename}_{systemname}_L_{L}_{u}_{Tmin}_{Tmax}.Tsweep`) with the following format

$$\begin{array}{cc}
 T[K], \kappa_{\text{nano}}^{\text{RTA}} \left[\frac{\text{W}}{\text{m} \cdot \text{K}} \right], & \kappa_{\text{nano}}^{\text{beyond RTA}} \left[\frac{\text{W}}{\text{m} \cdot \text{K}} \right] \\
 T_0, \kappa_{\text{nano}}^{\text{RTA}}(T_0), & \kappa_{\text{nano}}^{\text{beyondRTA}}(T_0) \\
 T_1, \kappa_{\text{nano}}^{\text{RTA}}(T_1), & \kappa_{\text{nano}}^{\text{beyondRTA}}(T_1) \\
 \vdots, \vdots, & \vdots \\
 T_n, \kappa_{\text{nano}}^{\text{RTA}}(T_n), & \kappa_{\text{nano}}^{\text{beyondRTA}}(T_n)
 \end{array}$$

where u is the transport direction.

Appendix B. Monte Carlo simulators and analyzers: inputs, outputs and executables

Appendix B.1. Geometry files

Files containing geometries are given in XML format. We provide a toy example to show geometry file input format:

```
<Geometry>
  <number_of_boxes Ngeom="4"/>
  <Box>
    <MaterialID name="black_P"/>
    <boxid id="0"/>
    <Vertices dim="2" npoints="4">
      6.0 6.0
      6.0 7.0
      7.0 6.0
      7.0 7.0
    </Vertices>
    <initCnd Teq="300."
      Tinit="301.0"/>
  </Box>
  <Box>
    <MaterialID name="black_P"/>
    <boxid id="1"/>
    <Vertices dim="2" npoints="4">
      6.0 6.0
      6.0 7.0
      5.0 6.0
      5.0 7.0
    </Vertices>
    <initCnd Teq="300."/>
  </Box>
```

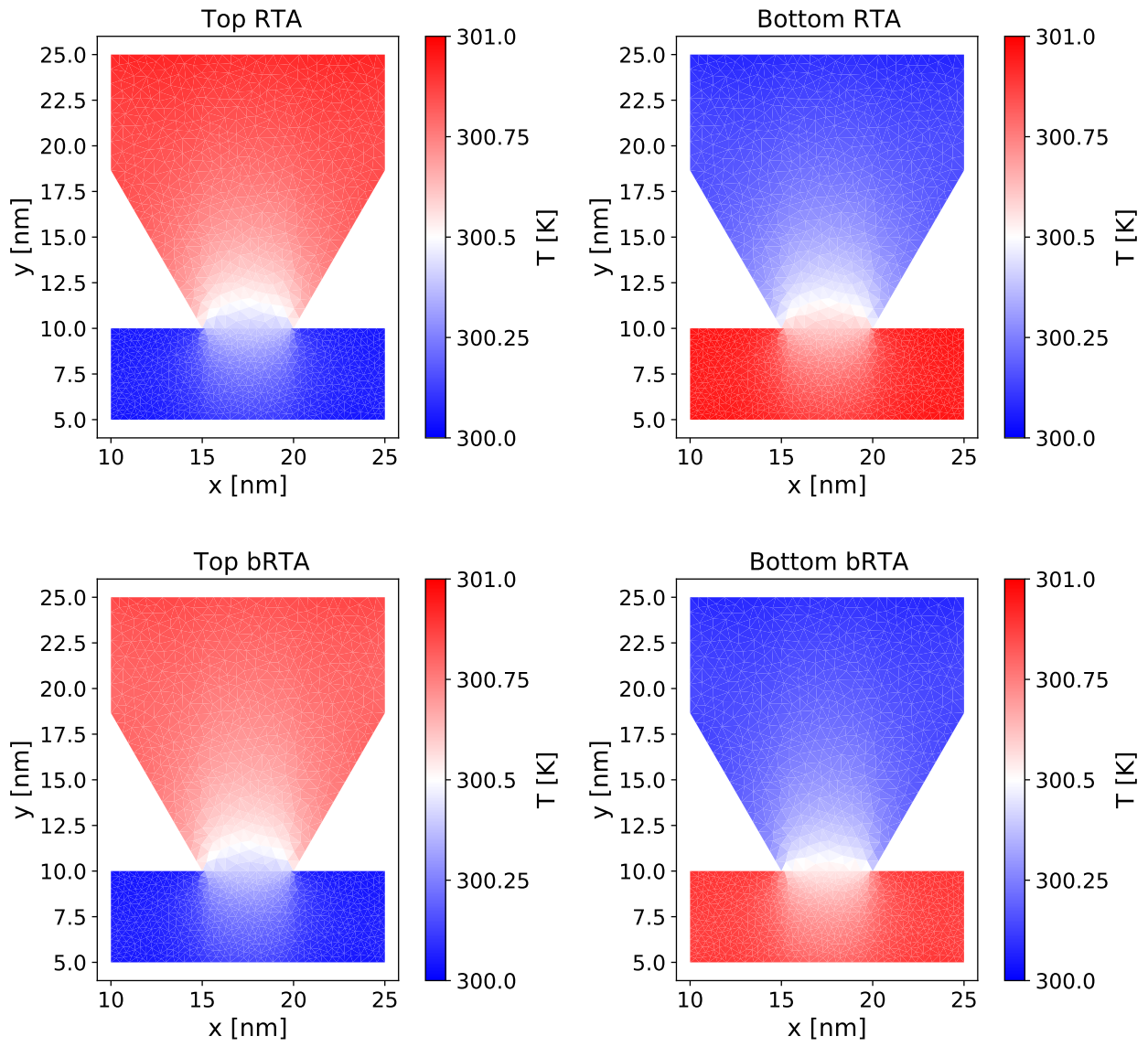


Figure 19: RTA and beyond RTA temperature profiles for Fig. 18 configurations at steady-state.

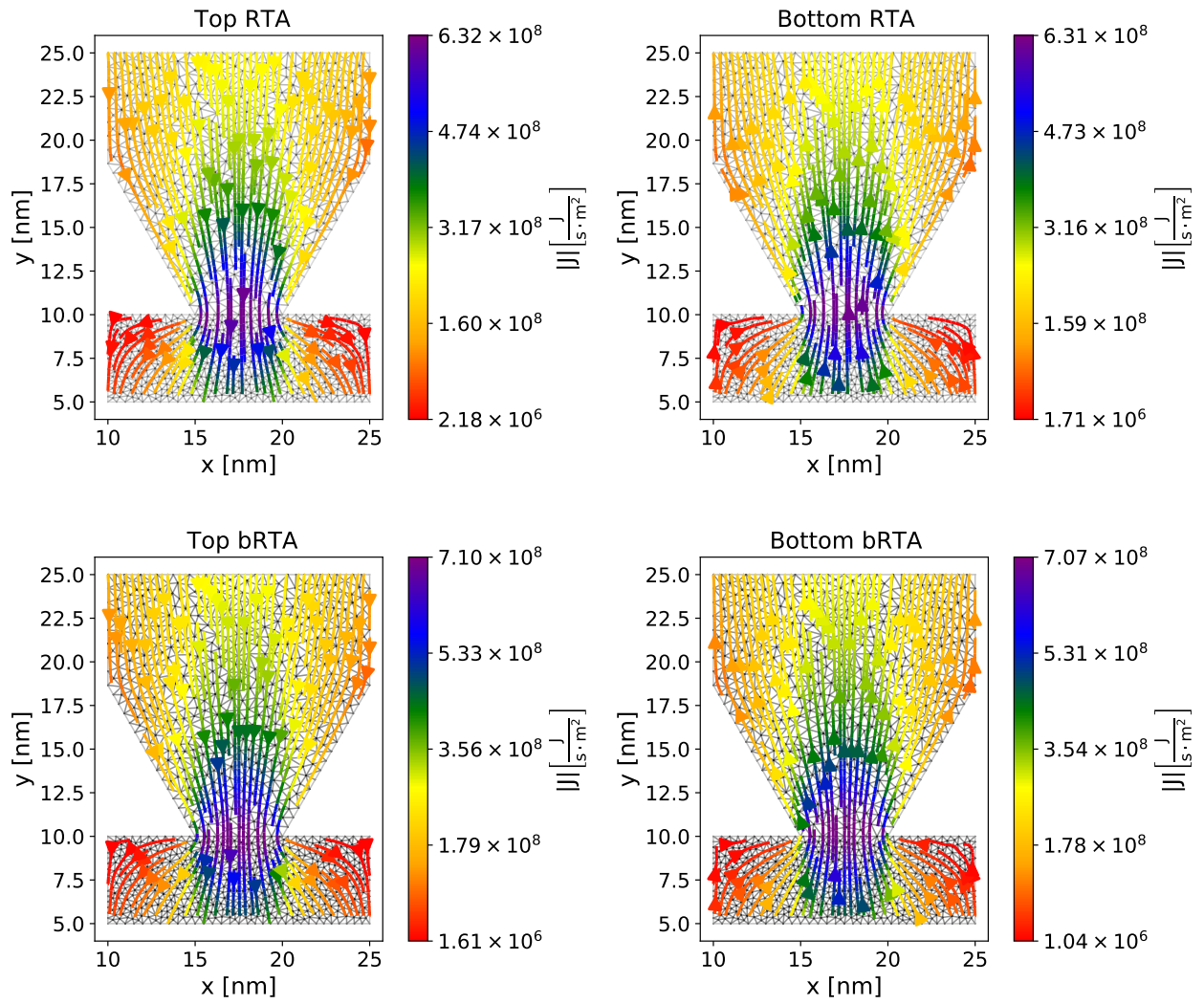


Figure 20: Steady-state RTA and beyond-RTA heat fluxes for the configurations depicted in Fig. 18.

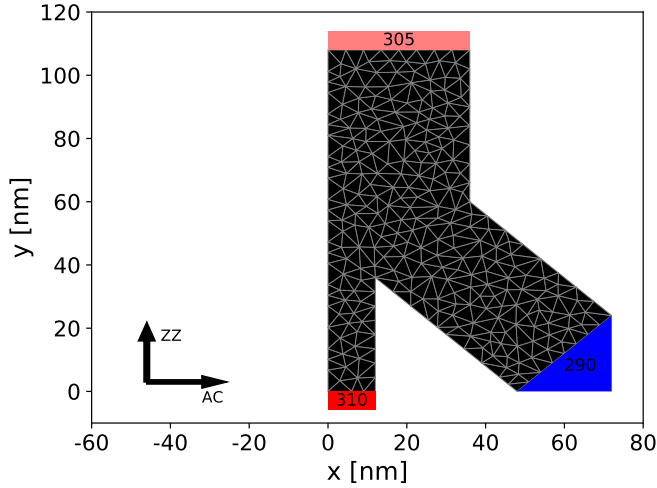


Figure 21: Example phosphorene structure with multiple terminals (isothermal reservoirs) at 310 K, 305 K and 290 K.

```

<Translate_to id="2">
    1.0 0.0 0.0
</Translate_to>
</Box>
<Box>
    <MaterialID name="black_P"/>
    <boxid id="2"/>
    <Vertices dim="2" npoints="4">
        8.0 6.0
        8.0 7.0
        7.0 6.0
        7.0 7.0
    </Vertices>
    <initCnd Teq="300."/>
    <Translate_to id="1">
        -1.0 0.0 0.0
    </Translate_to>
</Box>
<Box>
    <MaterialID name="black_P"/>
    <boxid id="3"/>
    <Vertices dim="2" npoints="4">
        5.0 6.0
        5.0 5.0
        8.0 6.0
        8.0 5.0
    </Vertices>
    <initCnd Teq="303.0"/>
    <Reservoir/>
</Box>
</Geometry>

```

We now list all possible parameters in geometry files:

1. number_of_boxes/Ngeom [integer]: Indicates the number of boxes.
2. Box/MaterialID/name [string]: Box material

3. Box/Vertices/dim [integer]: system dimension (Accepted values: 2).
4. Box/Vertices/npoints [integer]: number of vertices.
5. Box/Vertices [double, array(dim,npoints),units(nm)]: Box vertices (NOTE: they need to form a convex hull).
6. Box/initCnd/Teq [double,units(K)]: Reference temperature.
7. Box/initCnd/Tinit [double,optional,units(K)]: Temperature to initialize the box population out of reference (default: Teq). RTA simulator ignores this.
8. Box/Reservoir : if present it indicates that the box is an isothermal reservoir.
9. Box/Translate_to/id [int]: It indicates that any particle entering that box is translated to "id" box.
10. Box/Translate_to [double,array(1,3),units(nm)]: Translation vector applied to any particle entering that box.

Appendix B.2. RTAMC2D

The RTAMC2D executable implements the general RTA algorithm of Sec. 3.2 and the specialization described in Sec. 3.2.1 to obtain the steady-state for periodic structures under a thermal gradient. It has as command line inputs:

RTAMC2D input.xml N_{threads} [N_{runs}]

1. input.xml [string]: xml file containing the input.
2. N_{threads} [integer]: number of TBB threads for simulation.
3. N_{runs} [integer,optional]: number of repetitions to be done, to prevent table creation and data loading (default: 1).

Appendix B.2.1. input.xml

We provide now another toy example of input.xml files together with an explanation of its variables:

```

<RTA_MC2d>
    <geometry file="grta01.xml"/>
    <gradient x="0.2" y="0.0"/>
    <convergence energy="-1.0" flux="-1.0"/>
    <time dt="0.5" maxtime="100000"/>
    <material name="black_P"
        database="black_monolayer_50_50_1.h5"
        thickness="0.5" T0="300.0"/>
        <material name="biblack_P"
            database="biblack_50_50_1.h5"
            thickness="1.0" T0="300.0"/>
    <layer material="black_P"
        layer_name="black_bare"
        atoms="0 1 2 3"/>
    <layer material="biblack_P"
        layer_name="black_mid"
        atoms="0 1 2 3"/>
    <layer material="biblack_P"
        layer_name="black_alone"
        atoms="4 5 6 7"/>

```

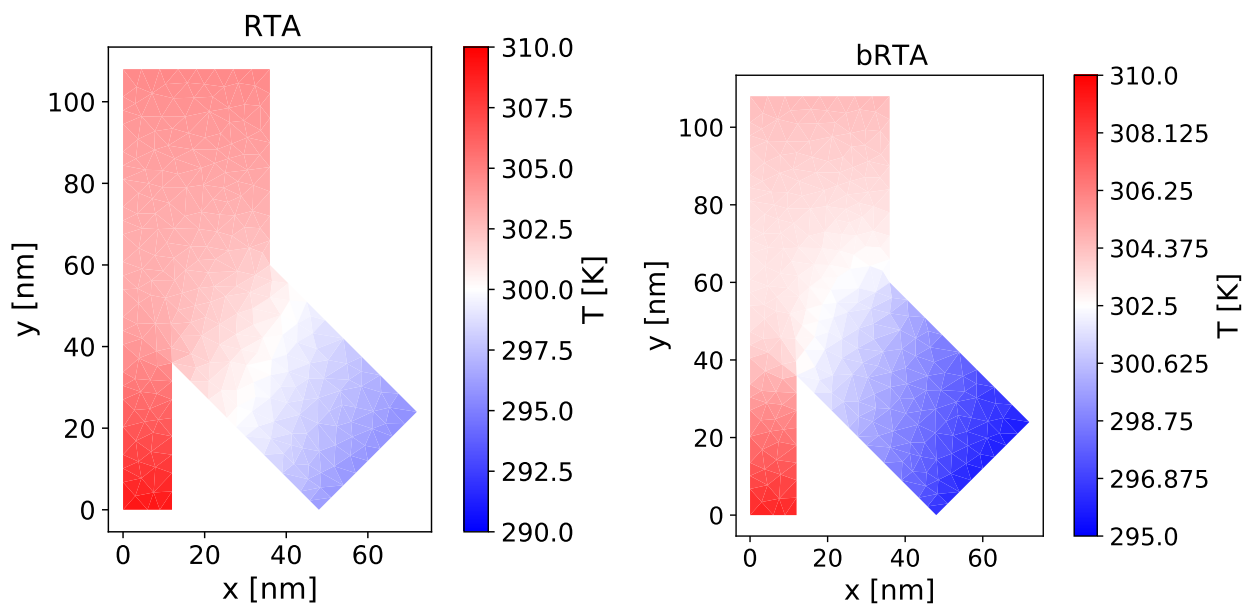


Figure 22: Steady-state RTA and beyond-RTA temperature profiles for the configuration depicted in Fig. 21.

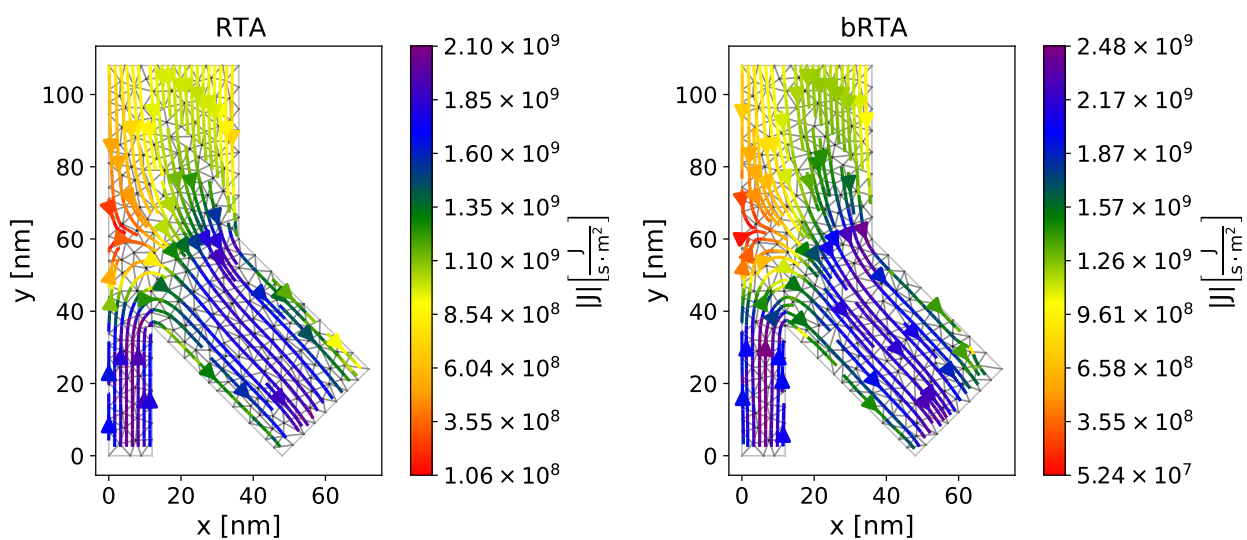


Figure 23: Steady-state RTA and beyond-RTA heat fluxes for the configuration depicted in Fig. 21.

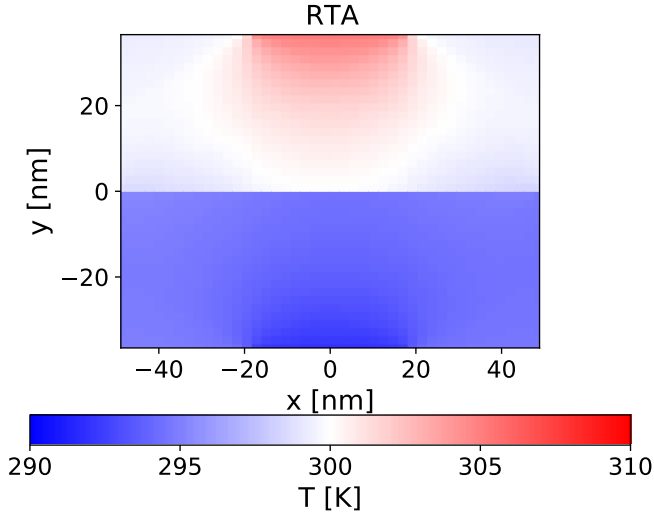


Figure 24: Steady-state RTA temperature profile for the configuration in Fig. 25.

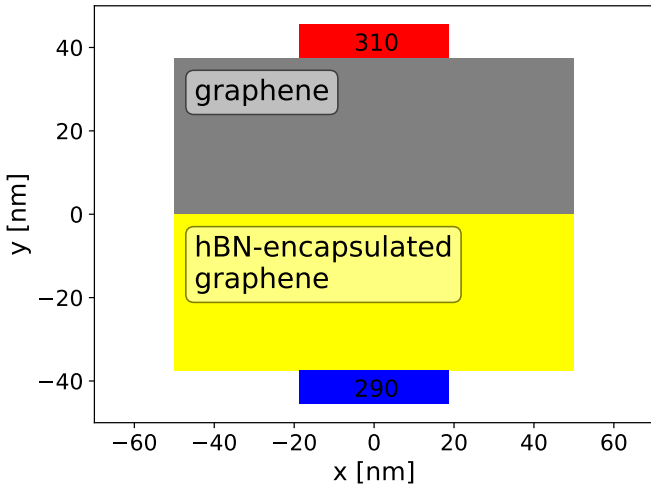


Figure 25: Structure containing a junction between graphene and hBN-encapsulated graphene and two isothermal boundaries at 290 K (blue) and 310 K (red).

```

<layers_connection layer_A="black_mid"
  layer_B="black_bare"/>
<particles N="10000000"/>
<ballistic/>
<spectral>
  <resolution ticks="500">
  <location bin="0">
</spectral/>
</RTA_MC2d>

```

1. geometry_file [string]: XML file containing geometry data.
2. gradient/x [double,units(K/nm)]: x-component of homogeneous thermal gradient applied to all boxes (NOTE: requires y-component and activates the specialized algorithm to obtain steady-state for extended systems).
3. gradient/y [double,units(K/nm)]: y-component of homogeneous thermal gradient applied to all boxes (NOTE: requires x-component and activates the specialized algorithm to obtain steady-state for extended systems).
4. convergence/energy [double,optional]: if given, the loop of the specialized algorithm to obtain steady-state for extended systems with an applied thermal gradient is broken when relative difference in deviational energy density is lower than this threshold (default: -1.0).
5. convergence/flux [double,optional]: if given, the loop of the specialized algorithm to obtain steady-state for extended systems with an applied thermal gradient is broken when relative differences of heat fluxes are lower than this threshold (default: -1.0).
6. time/dt [double,units(ps)]: spacing for mesh in time.
7. time/maxtime [double,units(ps)]: Maximum time for particles.
8. material/name [string]: material id.
9. material/database [string]: path to almaBTE's database containing phonon properties.
10. material/thickness [double,units(nm)]: real thickness in z-direction, used to correct DFT lattice vector in z-direction.
11. material/T0 [double,units(K)]: reference temperature of whole system (NOTE: it must be the same for all materials).
12. particles/N [integer]: Number of particles to be simulated (NOTE: be aware that even numbers are required for specialized algorithm to obtain steady-state for extended systems with an applied thermal gradient in order for sources not to add energy into the system).
13. spectral/resolution/ticks [integer,optional]: Number of divisions for spectral decomposition of fluxes and deviational temperature.
14. spectral/location/bin [integer,optional]: Box id in which spectral decomposition is calculated.

15. `layer/material` [string,optional]: name of material in which layer is localized. This is for LDMM.
16. `layer/layer_name` [string,optional]: name of layer. This is for LDMM.
17. `layer/atoms` [int,optional]: identity of atoms in the layer (follows the order of POSCAR). This is for LDMM.
18. `layers.connection/layer_A` [string,optional]: name of layer connected with `layer_B` (of same entry). There can be multiple entries of `layer.connection` if more than one connection is present. This is for LDMM.
19. `layers.connection/layer_B` [string,optional]: name of layer connected with `layer_A` (of same entry). This is for LDMM.
20. `ballistic` [optional]: if given, intrinsic scattering is deactivated.

Appendix B.2.2. Output files

In the case of specialized algorithm to obtain steady-state for periodic structures under thermal gradient a file called `steady_state_TOK_run_irun.csv`, where T_0 is the reference temperature and `irun` is the simulation id within the N_{runs} . This file contains in csv format the following:

$$\begin{array}{cccc} T_0, & T_1, & \dots, & T_{Nboxes} \\ J_{x,0}, & J_{x,1}, & \dots, & J_{x,Nboxes} \\ J_{y,0}, & J_{y,1}, & \dots, & J_{y,Nboxes} \end{array}$$

Additionally, if spectral decomposition is activated four files will be generated per selected box:

1. `steady_deltaT_omega_ibox_TOK_run_irun.csv`: contains the frequency grid in the first column and the deviational temperature per frequency in second one.
$$\begin{array}{cccc} \omega_0, & \omega_1, & \dots, & \omega_{Nticks} \\ \Delta T_0, & \Delta T_1, & \dots, & \Delta T_{Nticks} \end{array}$$
2. `steady_jx_omega_ibox_TOK_run_irun.csv`: analogous to temperature file, but with heat flux ($\text{J m}^{-2} \text{s}^{-1}$) in x-direction.
3. `steady_jy_omega_ibox_TOK_run_irun.csv`: analogous to temperature file, but with heat flux ($\text{J m}^{-2} \text{s}^{-1}$) in y-direction.
4. `steady_fd_q_ibox_TOK_run_irun.csv`: contains the q_x and q_y grid in the first and second rows, respectively, and the deviational phonon population per q -point in the following one.

$$\begin{array}{cccc} \#q_{x,0}, & q_{x,1}, & \dots, & q_{x,N_q-1} \\ \#q_{y,0}, & q_{y,1}, & \dots, & q_{y,N_q-1} \\ f^d(q_0), & f^d(q_1), & \dots, & f^d(q_{N_q-1}) \end{array}$$

On the other hand, the general algorithm produces three output files per run:

1. `temperature_TOK_run_irun.csv`: contains the temperature in K per boxes (column) at given times (rows). First column of each row gives the middle point of the time bin.

2. `jxTOK_run_irun.csv`: analogous to temperature file, but with heat flux ($\text{J m}^{-2} \text{s}^{-1}$) in x-direction.
3. `jyTOK_run_irun.csv`: analogous to temperature file, but with heat flux ($\text{J m}^{-2} \text{s}^{-1}$) in y-direction.

plus four additional files per selected box if spectral decomposition is conducted:

1. `deltaT_omega_ibox_TOK_run_irun.csv`: contains the frequency grid in the first column and the deviational temperature per frequency in at each time step in the following ones.

$$\begin{array}{cccc} -1, & \omega_0, & \omega_1, & \dots, & \omega_{Nticks} \\ t_0, & \Delta T_0(t_0), & \Delta T_1(t_0), & \dots, & \Delta T_{Nticks}(t_0) \\ t_1, & \Delta T_0(t_1), & \Delta T_1(t_1), & \dots, & \Delta T_{Nticks}(t_1) \\ \vdots & \vdots & \vdots & \ddots & \vdots \\ t_f, & \Delta T_0(t_f), & \Delta T_1(t_f), & \dots, & \Delta T_{Nticks}(t_f) \end{array}$$

where t_i is the middle point of each time grid bin.

2. `jx_omega_ibox_TOK_run_irun.csv`: analogous to temperature file, but with heat flux ($\text{J m}^{-2} \text{s}^{-1}$) in x-direction.
3. `jy_omega_ibox_TOK_run_irun.csv`: analogous to temperature file, but with heat flux ($\text{J m}^{-2} \text{s}^{-1}$) in y-direction.
4. `fd_q_ibox_TOK_run_irun.csv`: contains the q_x and q_y grid in the first and second rows, respectively, and the deviational phonon population per q -point at each time step in the following ones.

$$\begin{array}{cccc} \#q_{x,0}, & q_{x,1}, & \dots, & q_{x,N_q-1} \\ \#q_{y,0}, & q_{y,1}, & \dots, & q_{y,N_q-1} \\ t_1, & f^d(q_0, t_1), & \dots, & f^d(q_{N_q-1}, t_1) \\ \vdots & \vdots & \ddots & \vdots \\ t_f, & f^d(q_0, t_f), & \dots, & f^d(q_{N_q-1}, t_f) \end{array}$$

Appendix B.3. PropagatorBuilder

The `PropagatorBuilder` executable implements the building of the B -matrix and subsequent $P(\Delta t)$ calculation using the Krylov subspace method. It has as command line inputs:

```
[mpi] PropagatorBuilder database.h5 IFC3 T
      Δt Nthreads
```

1. `database.h5` [string]: `almABTE`'s database for that material.
2. `IFC3` [string]: third-order force constants file in sparse format [11].
3. `T` [double,units(K)]: reference temperature.
4. `Δt` [double, units(ps)]: time step for propagator calculation.
5. `Nthreads` [integer]: number of TBB threads to be used in the simulation.

Appendix B.3.1. Output files

PropagatorBuilder generate two binaries: `materialname_Na_Nb_1_TK_Δtps.B.eigen.bin` and `materialname_Na_Nb_1_TK_Δtps.P.eigen.bin`, which contain the B and $P(\Delta t)$ matrices.

Appendix B.4. beRTAMC2D

The `beRTAMC2D` executable implements the bRTA algorithm. It has the following command line inputs:

`beRTAMC2D input.xml Nthreads`

1. `input.xml` [string]: xml file containing the input.
2. `Nthreads` [integer]: number of TBB threads to be used in the simulation.

Appendix B.4.1. input.xml

We provide now another toy example of `input.xml` files together with an explanation of its variables:

```
<beRTAMC2D>
  <geometry file="grta01.xml"/>
  <gradient x="0.2" y="0.0"/>
  <time dt="0.5" maxtime="100000"/>
  <material name="black_P"
    database="black_monolayer_50_50_1.h5"
    thickness="0.5">
    <propagator T="300"
      file="bP.P.eigen.bin"/>
  </material>
  <Eeff Ed="4.0e-26" particles="3600"
    Tmax="301.0" Tmin="299.0"/>
</beRTAMC2D>
```

1. `geometry_file` [string]: XML file containing geometry data.
2. `gradient/x` [double,units(K/nm)]: x-component of homogeneous thermal gradient applied to all boxes (NOTE: requires y-component).
3. `gradient/y` [double,units(K/nm)]: y-component of homogeneous thermal gradient applied to all boxes (NOTE: requires x-component).
4. `time/dt` [double,units(ps)]: time step.
5. `time/maxtime` [double,units(ps)]: Maximum time for simulation.
6. `material/name` [string]: material id.
7. `material/database` [string]: path to `almaBTE`'s database containing phonon properties.
8. `material/thickness` [double,units(nm)]: real thickness in z-direction, used to correct DFT lattice vector in z-direction.
9. `material/propagator/T` [double,units(K)]: reference temperature used to calculate the propagator.
10. `material/propagator/file` [string]: path to propagator matrix binary.

11. `Eeff/particles` [integer]: division of energy guess, the calculation of the guess is done individually per box and the minimum value is selected. Not needed if `Eeff/Ed` is provided.
12. `Eeff/Tmin` [double,units(K)]: minimum temperature used to calculate the deviational energy per particle. Not needed if `Eeff/Ed` is provided.
13. `Eeff/Tmax` [double,units(K)]: maximum temperature used to calculate the deviational energy per particle. Not needed if `Eeff/Ed` is provided.
14. `Eeff/Ed` [double,units(J)]: deviational energy per particle, it is not needed if `Eeff/particles`, `Eeff/Tmin` and `Eeff/Tmax` are provided. (NOTE: the `RTAMC2D` calculated value for same system and initial conditions is a proper value).
15. `RTA` [optional]: if given, the RTA is used for scattering.

Appendix B.4.2. Outputs: standard output

Simulation data is dumped to standard output, with lines without physical information starting with `#`. Data for lines with physical information is structured as follows:

$$istep \ t \ N_{particles} \ \rho_0^d \ J_{x,0} \ J_{y,0} \ \dots \ \rho_{N-1}^d \ J_{x,N-1} \ J_{y,N-1},$$

with `istep` being the MC loop step, and the energy density and fluxes are given for the N boxes forming the system. All quantities are given in SI except for time which is given in ps.

Appendix B.4.3. Outputs: properties.msgpack.bin

The particle distribution per box and time step is dumped in sparse binary format in `properties.msgpack.bin` using `MessagePack` library [73]. Each time step information in the file starts by a `std::size_t` value (`size_block`) followed by `#` indicating the number of characters comprising the block. Blocks are comprised of arrays of $3 + 2N_{boxes}$ elements, with the three first ones being: time (double), deviational energy per particle (double) and one array with the T_{ref} for all boxes. This is followed by a structure for each box composed of an `std::size_t` indicating the number of non-zero elements in the distribution function vector and one array containing non-zero pairs (except in the case of empty boxes in which a dummy one is created) of an `std::size_t` indicating the phonon mode and one integer containing the number of net particles in that mode with its sign indicating if they are positive or negative particles. This file can be processed with `dist_reader` executable to obtain the spectral decomposition of the deviational temperature and heat flux at selected boxes and times.

Appendix B.5. dist_reader

The `dist_reader` executable allows the extraction of spectral resolved quantities. It has as command line inputs:

dist_reader input.xml properties.msgpack.bin

1. input.xml [string]: xml file containing the input.
2. properties.msgpack.bin [string]: file containing distribution function at given times as produced by beRTAMC2D.

it will provide the spectral decomposition of the deviational temperature as well as those of fluxes, with the same format as RTAMC2D spectral decomposition files, but with time column referring to instantaneous time rather than the middle of time bin.

Appendix B.5.1. input.xml

input.xml is the same as in the case of beRTAMC2D, with the following extra terms:

1. spectral/resolution/ticks [integer]: Number of divisions for spectral decomposition of fluxes and deviational temperature.
2. spectral/time/t [double]: Times at which the spectral decomposition will be calculated. It can be used more than one time
3. spectral/location/bin [integer]: Box id in which spectral decomposition is calculated. It can be used more than one time.

Appendix B.5.2. Output files

Spectral decomposition of temperature is printed in deltaT_omega_BoxID.csv and fluxes in jx_omega_BoxID.csv and jy_omega_BoxID.csv. The q -resolved deviational phonon distribution function is printed in fd_BoxID.csv. Data format is the same of the RTA spectral decomposed and q -resolved quantities, but this time with t indicating the instantaneous time and not the middle of time bin.

Appendix C. Suppression factors for nanowires

Suppression factors for nanowires (S_λ^{nw}) can be calculated, analogously to the case nanoribbons, by evaluating the integrals in Eq. 8 of Ref. 8 in cylindrical coordinates, yielding:

$$S_\lambda^{\text{nw}} = 1 - \frac{2M_\lambda^{\text{nw}}}{R^2} \left[M_\lambda^{\text{nw}} \left(e^{-\frac{R}{M_\lambda^{\text{nw}}}} - 1 \right) + R \right] \quad (\text{C.1})$$

$$M_\lambda^{\text{nw}} = \|v_\lambda - (v_\lambda \cdot u)u\| \tau_\lambda \quad (\text{C.2})$$

where R is the nanowire radius.

Appendix D. RTA algorithm

We now describe all possible events that a particle may take part of during the RTA simulation.

Appendix D.1. Particle generation

The deviational power introduced in the system is calculated as $|\dot{E}^{\text{tot}}| = |\dot{E}^{\nabla_r T}| + |\dot{E}^{\text{iso}}|$ where $|\dot{E}^{\nabla_r T}|$ and $|\dot{E}^{\text{iso}}|$ are the deviational power due to applied thermal gradients and isothermal walls, and are given by:

$$|\dot{E}^{\text{iso}}| = \sum_{j,i} |\dot{E}_{i,j}^{\text{iso}}| = \sum_{j,i} \frac{\delta z_j L_j}{N_q V_{\text{uc}}} |(n_i^0(T_j) - n_i^0(T_{\text{ref}}))| \times v_i \cdot \hat{e}_j^{\text{out}} \Theta(v_i \cdot \hat{e}_j^{\text{out}}), \quad (\text{D.1})$$

where j is the isothermal wall index, i runs over modes at the wall, δz_j is the material's thickness, L_j the wall length, N_q the number of q -points at which phonon properties are calculated, \hbar is the reduced Planck constant, V_{uc} is the unit cell volume and \hat{e}_j^{out} is a unit vector pointing outwards from the wall, and

$$|\dot{E}^{\nabla_r T}| = \sum_{j,i} |\dot{E}_{i,j}^{\nabla_r T}| = \sum_{j,i} \frac{V_{j,\text{box}}}{N_q V_{\text{uc}}} \times |v_i \cdot \nabla_r T| \frac{\partial n_i^0(T_{\text{ref}})}{\partial T}. \quad (\text{D.2})$$

Then particles with mode i are generated at j from source s with a probability $|\dot{E}_{i,j}^s|/|\dot{E}^{\text{tot}}|$ and $\sigma = \text{sgn}(E_{i,j}^s)$.

Appendix D.2. Free flight

Particles evolve ballistically from r_0 ($r_f = r_0 + v_i t_{\text{flight}}$) where t_{flight} is defined as $\min\{\tau_i \ln(R), t_b\}$, where t_b is the time the particle needs to encounter a boundary, interface or an isothermal wall and R is random number in range $(0, 1]$.

Appendix D.3. Interface scattering

If a particle arrives to an interface between two different materials we use the diffuse mismatch model [74, 75] to determine the output state and side in a $A - B$ interface as:

$$P_{k,A \rightarrow k',C} = \frac{8\pi^3}{V_{\text{uc},C} N_{q,C}} |v_k \cdot n| \delta(\omega'_k - \omega_k) \times \left(\Theta(v_k \cdot n) \delta_{BC} + \Theta(-v_k \cdot n) \delta_{AC} \right) \left/ \left[\sum_D^{A,B} \frac{8\pi^3}{V_{\text{uc},D} N_{q,D}} \sum_j |v_j \cdot n| \times \delta(\omega_j - \omega_k) (\Theta(v_j \cdot n) \delta_{BD} + \Theta(-v_j \cdot n) \delta_{AD}) \right] \right. \quad (\text{D.3})$$

where n is the vector normal to the interface, pointing out of A into B , and $C \in \{A, B\}$. For systems with layered stacks the LDMM of Section 3.2.2 can be used, thus multiplying the probability $P_{k,A \rightarrow k',C}$ by the coupling constant $\mathcal{C}_{k,k'}^{A,C}$

Appendix D.4. Boundary scattering

A particle encountering a boundary undergoes a full diffusive boundary scattering process after which the outgoing mode is determined following Lambert's cosine law [see Eq. (3)].

Appendix D.5. Absorption by reservoirs

Whenever a particle reaches a reservoir, it is absorbed by it, thus terminating its trajectory.

Appendix D.6. Intrinsic scattering

If particles end their free flight segment without encountering a boundary, interface or isothermal reservoir, they undergo intrinsic scattering, in which the phonon mode (k') is resampled from the distribution $\frac{C_{k'}(j)/\tau_{k'}(j)}{\sum_i C_i(j)/\tau_k(j)}$ of the j -th computational box.

Appendix D.7. Particle termination

Besides being terminated when contacting reservoirs, particles are also terminated if their simulation time exceeds a maximum threshold, in order to alleviate computational burden. This is justified as trajectories contributing to heat flux reach values in the order of the statistical deviation after a relatively small number of scattering events [19, 17].

Appendix E. Beyond RTA

Overall the implemented bRTA algorithm is quite similar to that of the RTA described in Appendix D except for scattering and sampling (see Sec. 3.3), as well as the following aspects:

1. Initial temperature: It allows for initial temperatures different to the reference one.
2. Free flight: t_{flight} is defined as $\min\{\Delta t, t_b\}$ being Δt the time step used for $P(\Delta t)$ calculation.
3. Interface scattering: It is not implemented.
4. Boundary scattering: Particles reaching the boundaries are used to calculate the boundary temperature (T_{wall}) via cubic spline interpolation of $E_{\text{out}}\Delta t/(L_{\text{border}}\delta z) = \frac{1}{V_{\text{uc}}} \sum_i v_i \cdot \hat{e}_{\perp}^{\text{in}} (n_i^0(T_{\text{wall}}) - n_i^0(T_{\text{ref}})) [v_i \cdot \hat{e}_{\perp}^{\text{in}} > 0]$, where \hat{e}_{\perp} is a vector normal to the boundary, pointing inside the material. Then, T_{wall} is used to create the distribution from which particles are randomly drawn during the time step.

Appendix E.1. Initial temperature

An initial number of particles is generated due to an initial temperature profile ($t = 0$ ps). The number of particles (N^j) introduced in the j -th box is calculated as:

$$N^j = \sum_i |N_i^j| = \sum_i \left| \frac{V_{j,\text{box}}}{N_q V_{\text{uc}} \varepsilon_d} \times (n_i^0(T_j) - n_i^0(T_{\text{ref}})) \right| \quad (\text{E.1})$$

where i is the phonon mode. Then particles with mode i are generated at j with a probability $|N_i^j|/N^j$ and $\sigma = \text{sgn}(N_i)$.

Appendix E.2. Particle cancellation

As the scattering step creates new particles, computational cost will scale to infinity as simulation progresses. That is prevented by a cancellation scheme in which particles in the same box and identical mode but with opposite sign are removed [30]. It should be noted that cancellation is not performed at each time step, but periodically, so as to achieve a balance between the increased number of particles and the cancellation cost.

Appendix E.3. Storage of particle distributions

A histogram of particles is saved at each time step, enabling the calculation of frequency- and mode-resolved properties. Writing to disk is handled by a dedicated thread and performed in a sparse format using the MessagePack library [73].

Appendix F. RTA-bRTA

The RTA version of the bRTA algorithm is exactly equal to the full version, except that the scattering algorithm for each particle in a given state k is simplified to generate a random number R in range $[0, 1)$ and if $R < 1 - e^{B_{kk}\Delta t}$ the particle is scattered and resampled from the distribution $\frac{C_{k'}(j)/\tau_{k'}(j)}{\sum_i C_i(j)/\tau_k(j)}$ of the j -th computational box. Contrary to the RTAMC2D implementation, this RTA implementation allows for multiple reference temperatures and initial temperature profiles. Despite those advantages, we notice that RTAMC2D implementation is much more efficient for steady-state calculations, with time-independent sources.

Appendix G. Thermal properties of phosphorene ZZ-nanoribbons

Here we provide, for reference, the results for the heat flux profiles and fits to the mesoscopic Eq. 22 of ZZ-nanoribbons having several widths under an applied thermal gradient. Those results (see Figs. G.26-G.29) do not provide any additional information regarding the analysis done in Sec. 5.1.1, with the AC findings and conclusions also valid for ZZ nanoribbons.

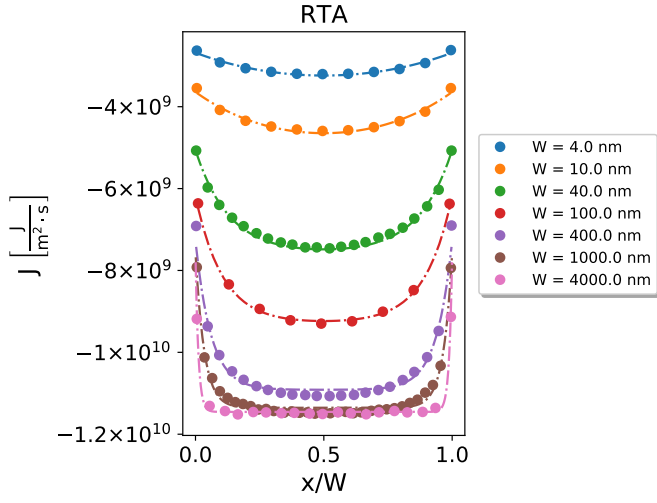


Figure G.26: Fitting to Eq. 22 (lines) of RTA-MC calculated heat flux (points) as a function of normalized position for phosphorene ZZ nanoribbons of different widths under the effect of $\nabla_{ZZ}T = 0.2 \text{ K nm}^{-1}$.

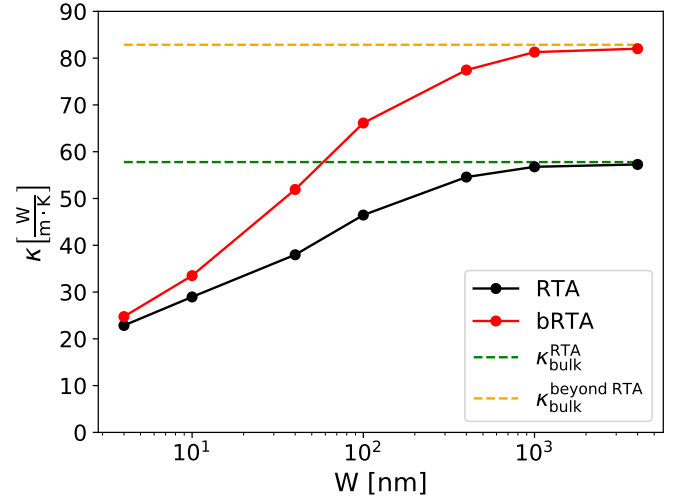


Figure G.28: Fitted thermal conductivity as a function of ZZ nanoribbon width for RTA (black) and bRTA (red) MC calculations. RTA (green) and beyond RTA (orange) bulk values are given for reference.

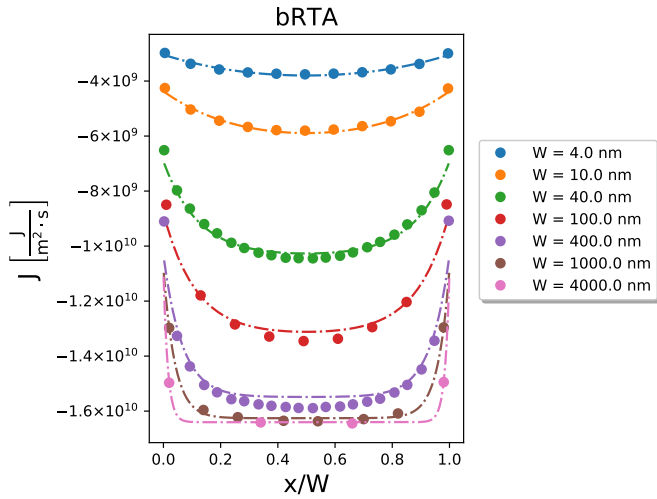


Figure G.27: Fitting to Eq. 22 (lines) of bRTA calculated heat flux (points) as a function of normalized position for phosphorene ZZ nanoribbons of different widths under the effect of $\nabla_{ZZ}T = 0.2 \text{ K nm}^{-1}$.

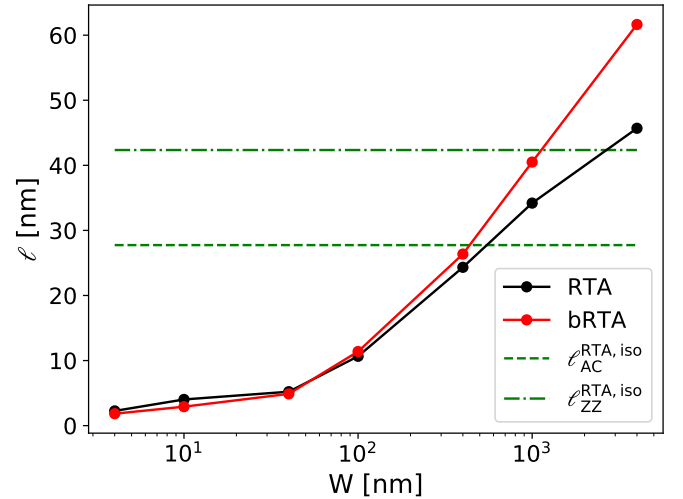


Figure G.29: Fitted non-local distance ℓ as a function of ZZ nanoribbon width for RTA (black) and bRTA (red) MC calculations. RTA bulk values of ℓ calculated using Sendra et. al.'s formula [55] are given for reference (green).

References

References

- [1] G. E. Moore, Cramming more components onto integrated circuits, *Electronics* 38 (1965) 114–117.
- [2] A. L. Moore, L. Shi, Emerging challenges and materials for thermal management of electronics, *Mater. Today* 17 (4) (2014) 163–174.
- [3] M. Chhowalla, D. Jena, H. Zhang, Two-dimensional semiconductors for transistors, *Nat. Rev. Mater.* 1 (11) (2016) 16052.
- [4] D. Akinwande, N. Petrone, J. Hone, Two-dimensional flexible nanoelectronics, *Nat. Commun.* 5 (1) (2014) 5678.
- [5] J. Jiang, K. Parto, W. Cao, K. Banerjee, Ultimate monolithic-3d integration with 2d materials: Rationale, prospects, and challenges, *IEEE J. Electron Devices Soc.* 7 (2019) 878–887.
- [6] J. M. Ziman, *Electrons and Phonons: The Theory of Transport Phenomena in Solids*, Oxford Classic Texts in the Physical Sciences, Oxford University Press, Oxford, 2001.
- [7] M. Omini, A. Sparavigna, Beyond the isotropic-model approximation in the theory of thermal conductivity, *Phys. Rev. B* 53 (1996) 9064–9073.
- [8] W. Li, N. Mingo, L. Lindsay, D. A. Broido, D. A. Stewart, N. A. Katcho, Thermal conductivity of diamond nanowires from first principles, *Phys. Rev. B* 85 (2012) 195436.
- [9] A. Ward, D. A. Broido, D. A. Stewart, G. Deinzer, Ab initio theory of the lattice thermal conductivity in diamond, *Phys. Rev. B* 80 (2009) 125203.
- [10] L. Lindsay, D. A. Broido, T. L. Reinecke, Ab initio thermal transport in compound semiconductors, *Phys. Rev. B* 87 (2013) 165201.
- [11] W. Li, J. Carrete, N. A. Katcho, N. Mingo, Shengbte: A solver of the boltzmann transport equation for phonons, *Comput. Phys. Commun.* 185 (6) (2014) 1747–1758.
- [12] J. Carrete, B. Vermeersch, A. Katre, A. van Roekeghem, T. Wang, G. K. Madsen, N. Mingo, almabte : A solver of the space–time dependent boltzmann transport equation for phonons in structured materials, *Comput. Phys. Commun.* 220 (2017) 351–362.
- [13] A. Togo, L. Chaput, I. Tanaka, Distributions of phonon lifetimes in brillouin zones, *Phys. Rev. B* 91 (2015) 094306.
- [14] Y. Chen, D. Li, J. R. Lukes, A. Majumdar, Monte Carlo Simulation of Silicon Nanowire Thermal Conductivity, *J. Heat Transf.* 127 (10) (2005) 1129–1137.
- [15] S. Mei, L. N. Maurer, Z. Aksamija, I. Knezevic, Full-dispersion monte carlo simulation of phonon transport in micron-sized graphene nanoribbons, *J. Appl. Phys.* 116 (16) (2014) 164307.
- [16] V. Jean, S. Fumeron, K. Termentzidis, S. Tutashkonko, D. Lacroix, Monte carlo simulations of phonon transport in nanoporous silicon and germanium, *J. Appl. Phys.* 115 (2) (2014) 024304.
- [17] J.-P. M. Péraud, C. D. Landon, N. G. Hadjiconstantinou, Monte carlo methods for solving the boltzmann transport equation, *Annu. Rev. Heat Transf.* 17.
- [18] J.-P. M. Péraud, N. G. Hadjiconstantinou, Efficient simulation of multidimensional phonon transport using energy-based variance-reduced monte carlo formulations, *Phys. Rev. B* 84 (2011) 205331.
- [19] J.-P. M. Péraud, N. G. Hadjiconstantinou, An alternative approach to efficient simulation of micro/nanoscale phonon transport, *Appl. Phys. Lett.* 101 (15) (2012) 153114.
- [20] A. Cepellotti, G. Fugallo, L. Paulatto, M. Lazzeri, F. Mauri, N. Marzari, Phonon hydrodynamics in two-dimensional materials, *Nat. Commun.* 6 (1) (2015) 6400.
- [21] L. Lindsay, A. Katre, A. Cepellotti, N. Mingo, Perspective on ab initio phonon thermal transport, *J. Appl. Phys.* 126 (5) (2019) 050902.
- [22] C. Landon, N. Hadjiconstantinou, Deviation simulation of phonon transport in graphene ribbons with ab initio scattering, *J. Appl. Phys.* 116 (2014) 163502.
- [23] Boost geometry, https://www.boost.org/doc/libs/1_70_0/libs/geometry/doc/html/index.html, accessed: 2021-04-30.
- [24] F. F. M. Sabatti, S. M. Goodnick, M. Saraniti, Simulation of Phonon Transport in Semiconductors Using a Population-Dependent Many-Body Cellular Monte Carlo Approach, *J. Heat Transf.* 139 (3), 032002.
- [25] J. Randrianalisoa, D. Baillis, Monte carlo simulation of cross-plane thermal conductivity of nanostructured porous silicon films, *J. Appl. Phys.* 103 (5) (2008) 053502.
- [26] J. Randrianalisoa, D. Baillis, Monte Carlo Simulation of Steady-State Microscale Phonon Heat Transport, *J. Heat Transf.* 130 (7), 072404.
- [27] W. Xu, G. Zhang, B. Li, Interfacial thermal resistance and thermal rectification between suspended and encased single layer graphene, *J. Appl. Phys.* 116 (13) (2014) 134303.
- [28] X.-K. Chen, M. Pang, T. Chen, D. Du, K.-Q. Chen, Thermal rectification in asymmetric graphene/hexagonal boron nitride van der waals heterostructures, *ACS Appl. Mater. Interfaces* 12 (13) (2020) 15517–15526.
- [29] S.-i. Tamura, Isotope scattering of dispersive phonons in ge, *Phys. Rev. B* 27 (1983) 858–866.
- [30] C. D. Landon, A deviation monte carlo formulation of ab initio phonon transport and its application to the study of kinetic effects in graphene ribbons, Ph.D. thesis, Massachusetts Institute of Technology, Cambridge, MA (2014).
- [31] Conservation energy deltas are approximated by Gaussian functions ($\delta(\omega_i \pm \omega_j - \omega_k) \approx \frac{1}{\sqrt{2\pi}\sigma_{ijk}} \exp\left(-\frac{(\omega_i \pm \omega_j - \omega_k)^2}{2\sigma_{ijk}^2}\right)$) with $\sigma_{ijk} = \frac{a}{\sqrt{12}} \|(G_{\mu\alpha}^T N_{\mu\mu}^{-1})^T \cdot (\mathbf{v}_j - \mathbf{v}_k)_\alpha\|$, where i, j and k are the phonon modes taking part in the three-phonon process, μ indicates a reciprocal-space lattice vector, α indicates a cartesian axis, $G_{\mu\alpha}$ is the reciprocal lattice, $N_{\mu\mu}$ is a diagonal matrix with the q-grid size and a is the scalebroad factor) which, because of how σ_{ijk} is calculated, breaks the microscopic reversibility as one process can be registered but not the reciprocal or it can be registered, but with different value. Moreover, the way smearing is constructed from products of velocities over reciprocal lattice vectors can cause symmetry equivalent pairs/triplets to give different values.
- [32] A. Neumaier, Rundungsfehleranalyse einiger verfahren zur summation endlicher summen, *ZAMM-Z. Angew. Math. Me.* 54 (1) (1974) 39–51.
- [33] C. Moler, C. Van Loan, Nineteen dubious ways to compute the exponential of a matrix, twenty-five years later, *SIAM Rev.* 45 (1) (2003) 3–49.
- [34] N. J. Higham, The scaling and squaring method for the matrix exponential revisited, *SIAM Rev.* 51 (4) (2009) 747–764.
- [35] Eigen3 exponential matrix, https://eigen.tuxfamily.org/dox/unsupported/group_MatrixFunctions_Module.html#matrixbase_exp, accessed: 2021-04-30.
- [36] W. E. Arnoldi, The principle of minimized iterations in the solution of the matrix eigenvalue problem, *Q. Appl. Math.* 9 (1) (1951) 17–29.
- [37] C. Wasshuber, About single-electron devices and circuits, Ph.D. thesis, Technische Univ. Wien, Vienna, AT (1997).
- [38] Y. Saad, Analysis of some krylov subspace approximations to the matrix exponential operator, *SIAM J. Numer. Anal.* 29 (1) (1992) 209–228.
- [39] Q. H. Wang, K. Kalantar-Zadeh, A. Kis, J. N. Coleman, M. S. Strano, Electronics and optoelectronics of two-dimensional transition metal dichalcogenides, *Nat. Nanotechnol.* 7 (11) (2012) 699–712.
- [40] F. Schwierz, Graphene transistors, *Nat. Nanotechnol.* 5 (7) (2010) 487.
- [41] S. Chen, S. Kim, W. Chen, J. Yuan, R. Bashir, J. Lou, A. M. van der Zande, W. P. King, Monolayer mos2 nanoribbon transistors fabricated by scanning probe lithography, *Nano Lett.* 19 (3) (2019) 2092–2098.
- [42] N. Haratipour, S. Namgung, S.-H. Oh, S. J. Koester, Fundamental limits on the subthreshold slope in schottky source/drain black phosphorus field-effect transistors, *ACS Nano* 10 (3) (2016) 3791–3800, PMID: 26914179.
- [43] X. Luo, Y. Rahbariagh, J. C. M. Hwang, H. Liu, Y. Du, P. D.

- Ye, Temporal and thermal stability of al₂o₃-passivated phosphorene mosfets, *IEEE Electron Device Lett.* 35 (12) (2014) 1314–1316.
- [44] L. Li, Y. Yu, G. J. Ye, Q. Ge, X. Ou, H. Wu, D. Feng, X. H. Chen, Y. Zhang, Black phosphorus field-effect transistors, *Nat. Nanotechnol.* 9 (5) (2014) 372–377.
- [45] P. Wu, D. Reis, X. S. Hu, J. Appenzeller, Two-dimensional transistors with reconfigurable polarities for secure circuits, *Nat. Electron.* 4 (1) (2021) 45–53.
- [46] H. Ilatikhameneh, T. Ameen, B. Novakovic, Y. Tan, G. Klimeck, R. Rahman, Saving moore’s law down to 1 nm channels with anisotropic effective mass, *Sci. Rep.* 6 (1) (2016) 31501.
- [47] B. Smith, B. Vermeersch, J. Carrete, E. Ou, J. Kim, N. Mingo, D. Akinwande, L. Shi, Temperature and thickness dependences of the anisotropic in-plane thermal conductivity of black phosphorus, *Adv. Mater.* 29 (5) (2017) 1603756.
- [48] J. Carrete, W. Li, L. Lindsay, D. A. Broido, L. J. Gallego, N. Mingo, Physically founded phonon dispersions of few-layer materials and the case of borophene, *Mater. Res. Lett.* 4 (4) (2016) 204–211.
- [49] A. Castellanos-Gomez, L. Vicarelli, E. Prada, J. O. Island, K. L. Narasimha-Acharya, S. I. Blanter, D. J. Groenendijk, M. Buscema, G. A. Steele, J. V. Alvarez, H. W. Zandbergen, J. J. Palacios, H. S. J. van der Zant, Isolation and characterization of few-layer black phosphorus, *2D Mater.* 1 (2) (2014) 025001.
- [50] D. Zhao, X. Qian, X. Gu, S. A. Jajja, R. Yang, Measurement Techniques for Thermal Conductivity and Interfacial Thermal Conductance of Bulk and Thin Film Materials, *J. Electron. Packaging* 138 (4), 040802.
- [51] L. Zhu, G. Zhang, B. Li, Coexistence of size-dependent and size-independent thermal conductivities in phosphorene, *Phys. Rev. B* 90 (2014) 214302.
- [52] A. Jain, A. J. H. McGaughey, Strongly anisotropic in-plane thermal transport in single-layer black phosphorene, *Sci. Rep.* 5 (1) (2015) 8501.
- [53] S. Lee, D. Broido, K. Esfarjani, G. Chen, Hydrodynamic phonon transport in suspended graphene, *Nat. Commun.* 6 (1) (2015) 6290.
- [54] A. Sellitto, I. Carlomagno, D. Jou, Two-dimensional phonon hydrodynamics in narrow strips, *Proc. R. Soc. A: Math. Phys. Eng. Sci.* 471 (2182) (2015) 20150376.
- [55] L. Sendra, A. Beardo, P. Torres, J. Bafaluy, F. X. Alvarez, J. Camacho, Derivation of a hydrodynamic heat equation from the phonon boltzmann equation for general semiconductors, *Phys. Rev. B* 103 (2021) L140301.
- [56] K. Bernstein, R. K. Cavin, W. Porod, A. Seabaugh, J. Welsler, Device and architecture outlook for beyond cmos switches, *Proc. IEEE* 98 (12) (2010) 2169–2184.
- [57] A. J. Minnich, G. Chen, S. Mansoor, B. S. Yilbas, Quasiballistic heat transfer studied using the frequency-dependent boltzmann transport equation, *Phys. Rev. B* 84 (2011) 235207.
- [58] B. Vermeersch, J. Carrete, N. Mingo, A. Shakouri, Superdiffusive heat conduction in semiconductor alloys. i. theoretical foundations, *Phys. Rev. B* 91 (2015) 085202.
- [59] Y. Wang, A. Vallabhaneni, J. Hu, B. Qiu, Y. P. Chen, X. Ruan, Phonon lateral confinement enables thermal rectification in asymmetric single-material nanostructures, *Nano Lett.* 14 (2) (2014) 592–596, pMID: 24393070.
- [60] J. Lee, V. Varshney, A. K. Roy, J. B. Ferguson, B. L. Farmer, Thermal rectification in three-dimensional asymmetric nanostructure, *Nano Lett.* 12 (7) (2012) 3491–3496, pMID: 22716162.
- [61] C. Dames, Solid-State Thermal Rectification With Existing Bulk Materials, *J. Heat Transfer* 131 (6), 061301.
- [62] X. Cartoixà, L. Colombo, R. Rurali, Thermal rectification by design in telescopic si nanowires, *Nano Lett.* 15 (12) (2015) 8255–8259.
- [63] almbte database, <https://almbte.bitbucket.io/database/>, accessed: 2021-09-30.
- [64] J. P. Perdew, K. Burke, M. Ernzerhof, Generalized gradient approximation made simple, *Phys. Rev. Lett.* 77 (1996) 3865–3868.
- [65] S. Grimme, J. Antony, S. Ehrlich, H. Krieg, A consistent and accurate ab initio parametrization of density functional dispersion correction (dft-d) for the 94 elements h-pu, *J. Chem. Phys.* 132 (15) (2010) 154104.
- [66] S. Grimme, S. Ehrlich, L. Goerigk, Effect of the damping function in dispersion corrected density functional theory, *J. Comput. Chem.* 32 (7) (2011) 1456–1465.
- [67] G. Kresse, J. Hafner, Ab initio molecular dynamics for liquid metals, *Phys. Rev. B* 47 (1993) 558–561.
- [68] G. Kresse, J. Hafner, Ab initio molecular-dynamics simulation of the liquid-metal–amorphous-semiconductor transition in germanium, *Phys. Rev. B* 49 (1994) 14251–14269.
- [69] G. Kresse, J. Furthmüller, Efficiency of ab-initio total energy calculations for metals and semiconductors using a plane-wave basis set, *Comput. Mater. Sci.* 6 (1) (1996) 15 – 50.
- [70] A. Togo, I. Tanaka, First principles phonon calculations in materials science, *Scr. Mater.* 108 (2015) 1–5.
- [71] R. S. Pease, An x-ray study of boron nitride, *Acta Crystallogr.* 5 (3) (1952) 356–361.
- [72] D. Golla, K. Chattrakun, K. Watanabe, T. Taniguchi, B. J. LeRoy, A. Sandhu, Optical thickness determination of hexagonal boron nitride flakes, *Appl. Phys. Lett.* 102 (16) (2013) 161906.
- [73] Messagepack, <https://msgpack.org/>, accessed: 2021-04-30.
- [74] E. T. Swartz, R. O. Pohl, Thermal boundary resistance, *Rev. Mod. Phys.* 61 (1989) 605–668.
- [75] P. Reddy, K. Castelino, A. Majumdar, Diffuse mismatch model of thermal boundary conductance using exact phonon dispersion, *Appl. Phys. Lett.* 87 (21) (2005) 211908.